Surfaces and Interfaces 18 (2020) 100456

Contents lists available at ScienceDirect

Surfaces and Interfaces

journal homepage: www.elsevier.com/locate/surfin

Ceria doped CuMnOx as carbon monoxide oxidation catalysts: Synthesis and their characterization

Subhashish Dey*, Ganesh Chandra Dhal

Department of Civil Engineering, IIT (BHU), Varanasi, India

ARTICLE INFO

Keywords:
Ceria
CuMnOx catalyst
Carbon monoxide
Co-precipitation method
Characterization and reactive calcinations

ABSTRACT

The CuMnOx and ceria doped CuMnOx catalysts (with ceria loadings in the range 0.5–3 wt.%) were synthesized by using the Co-precipitation method and characterized by various methods as discussed in the manuscript. Carbon monoxide (CO) is an individual one of the most toxic gases presents in the atmosphere and ambient-temperature complete oxidation of it is an important process for human health protection. According to the results, Ceria was doped successfully into the CuMnOx catalyst lattice. The better catalytic activity was observed 2.50 wt.% of ceria doping in the CuMnOx catalyst was found. The calcinations strategies (reactive calcinations and traditional calcinations) of the precursor have a huge impact on the activity of resulting catalysts. The presence of more number of oxygen vacancies and high specific surface area in ceria promoted CuMnOx catalyst to design highly active catalyst. The reusability of ceria doped CuMnOx catalyst was also tested and observed that this catalyst does not show any high level of major changes in its catalytic activity even after reuses.

1. Introduction

Stabilization of base metals at low oxidation state is very important in their application of heterogeneous catalysts. These materials structured units often have represented the physical and chemical properties that are especially useful for their efficient applications. It's an economical, environmentally friendly and easily available catalyst for low-temperature CO oxidation [1,2]. These catalysts are synthesized via various methods and often produce several micro/ nanostructures with smart shapes, such as spherical, pyramids, laminated-cube and dumb-bell structures had been reported [3,4]. It is highly new investigated candidates due to their prospective application in catalysis and energy exchange [5]. Carbon monoxide (CO) is an individual one of the major toxic gases present in the atmosphere and produced from the partial oxidation of carbon-containing compounds [6]. CO combines with hemoglobin present in the blood cells and converted into carboxy-hemoglobin which reduces the oxygen carrying capacity of human body [7]. It is major reactive trace gases present in the earth's atmosphere, influences the atmospheric chemistry as well as the climate. The huge amounts of CO are emitted in the world, mainly from the transportation sector [8,9]. Rising the number of vehicles on roads, CO concentration has reached at alarming level in urban areas [10]. A catalytic converter is an emission control device that converts more toxic pollutants present in the automobile exhaust into less toxic by catalytic reactions [11]. It's also applications in housing, CO detectors, automotive air cleaning technologies, gas masks for firefighters and mining industry [12]. The performance of catalytic converter highly depends upon the types of catalysts was used. In the presence of catalyst, the rate of chemical reaction was increased; it acts like an agent that reduces the activation energy of reactions [13,14]. This mussel-inspired surface chemistry has invigorated great interest in material surface function of different materials and provides convenient shortcut to tailor the physicochemical properties for different applications.

A variety of transition metals and metal oxides catalysts have been investigated for the catalytic oxidation of CO, among them the CuMnOx catalyst was found to be more effective, which have shown that the excellent catalytic activities for such reactions. The hopcalite (CuMnOx) is one of the oldest known catalysts for CO oxidation at a low temperature. It was attracted much attention because of their low cost, high catalytic activity and moisture resistance [15]. In 1920 Lamb, Bray and Frazer discovered that various mixture oxides of Cu, Mn, Ag, and Co, identified as a group of catalysts known as hopcalite (CuMnOx). Jones and Taylor confirmed the catalytic properties of such a system called hopcalite in the year 1923. It can efficiently catalyze the oxidation of dry CO even at room temperature [16]. To date, there are various methods have been applied to synthesize the CuMnOx catalysts [17]. A literature survey reported that the hopcalite catalyst is highly active in the amorphous state even at room temperature but has been

* Corresponding author.
E-mail address: shubhashish.rs.civ13@itbhu.ac.in (S. Dey).

https://doi.org/10.1016/j.surfin.2020.100456
Received 27 November 2019; Received in revised form 21 January 2020; Accepted 22 January 2020
Available online 23 January 2020

observed to lose their activity after exposition at temperatures above 773 K where crystallization of the spinel $CuMn_2O_4$ has occurred. [18]. The addition of dopant into the CuMnOx catalyst improves their catalytic activity for CO oxidation. A lot of attention has been given to modification of the hopcalite catalyst to remove its faults of moisture deactivation and lower activity [19,20].

The distinct reaction mechanisms of CuMnOx catalyst with CO have been discussed below. In the CO oxidation process, the oxygen is first adsorbed on the CuMnOx catalyst surface with the energy of activation [21]. The Cu-oxide is found weakly active for CO oxidation, but in combination with Mn-oxide in suitable proportions, some very highly active catalyst system was generated [22]. It has been reported that these catalysts' have high catalytic activity in CO oxidation could be attributed to the resonance system $Cu^{2+} + Mn^{3+} \leftrightarrows Cu^{+} + Mn^{4+}$ and high adsorption of CO onto Cu^{2+}/Mn^{4+} and O_2 onto Cu^{+}/Mn^{3+}. The additional of Cu into MnOx improved its catalytic activity for CO oxidation [23,24]. The oxygen species associated with Cu in the CuMnOx catalyst are very active and may be dominated by the low-temperature catalytic oxidation of CO. In characterization points to improve the reactivity of lattice oxygen associated with Cu species as well as the mobility of lattice oxygen from Mn species [25,26]. Ceria had a high oxygen storage capacity and high redox properties; therefore, it was making more oxygen available for CO oxidation process. Ceria acts as reducible oxide support, improving the catalytic activity via metal-support interaction and/or improved dispersion of active metal components [27]. The thermo-dynamic study also represents that the endothermic nature of adsorption process. On the whole design and production of CuMnOx catalysts with high adsorption capacity are proved very facile and attractive for further used in other fields.

Each released O atom leaves a vacancy and creates two Ce^{3+} (Ce4f) cations by transferring electrons to two Ce^{4+} cations (Ce4f0). An important property of ceria has stabilized the catalyst against deactivation due to the high thermal stability and/or better dispersion of active metal [28]. Instead of using ceria alone as the catalyst for CO oxidation, more researchers focus on the modification of CeO_2 with different ions to improve the activity and thermal stability [29]. In the Ce doped CuMnOx catalyst, the presence of mixed oxides of Cu, Ce and Mn were the most enriched Mn^{4+} has the smallest size among all the cations present on the surface. Recent reports have shown that the activity of ceria in the complete CO oxidation processes can highly improved by the transition metals [30]. The CuMnCe catalyst has different morphological states of their elements and oxygen activation performances were synthesized by the co-precipitation method and impudence of their structural and redox properties on CO oxidation processes were investigated [31,32]. The ceria doped CuMnOx catalyst also influence by the ceria over yields of catalytic oxidation of CO. The Ce (III) and Ce (IV) have a high oxygen storage capacity which improves the catalytic potential, also its oxidation capacity of Ce^{3+} to Ce^{4+} states leads to high oxygen mobility resulting in better catalytic performance [34]. It is well-known that the modification of ceria by doping with transition metal cations induces several benefits on the catalytic features of ceria such as improvement in the thermal stability, enhanced surface reducibility, high oxygen mobility, which contributes to the effective CO oxidation [35]. Ceria is irreplaceable or its ability to be reduced and reoxidized, as well as oxygen mobility due to the rich bulk oxygen vacancies [36]. The performance of catalysts very much depends upon the calcinations conditions of precursors and subsequent pretreatment of the catalysts. The high-temperature calcinations cause sintering of active crystallites with a consequent loss of surface area and adverse effects on the performance of catalyst [37]. Therefore, to minimize the above mentioned drawbacks of two steps of calcinations and pretreatment, a newer route of single step thermal treatment of precursors in a reactive 4.5%CO–air mixture at a low temperature (160 °C) has been applied by the authors for preparing of highly active catalysts by passing the separate pretreatment step [38]. Such a single step thermal treatment of precursor is so-called "RC method" by the authors. It is postulated that during the RC method parallel to the multifarious phenomena of CO oxidation and precursor decomposition, it causes synergistic effect in the formation of oxygen-deficient catalyst at low temperature [39]. The success of catalysts has prompted a great deal of fundamental work devoted to clarifying the role played by each element and nature of active sites [40]. Therefore, the series of ceria doped CuMnOx catalyst were prepared for further research. The various catalysts were prepared by altering the w/w% of ceria doping on CuMnOx, which were characterized by SEM-EDX, XRD, FTIR, XPS, TEM and BET techniques. The catalytic activities of prepared catalysts evaluated and conversion of CO were monitored by the gas chromatography. The investigated materials were prepared by Co-precipitation method and pure CeO_2 sample was also prepared under identical conditions for comparison purposes [41,42]. A comparison of characteristics of fresh catalyst and spent catalysts has been conducted. If the spent catalysts can be regenerated, activated effectively and increase the life of catalyst, they can be reused with higher values and economic efficiency. The physical properties of spent catalysts, as well as their composition are generally different from those of fresh catalysts [43,44]. Along with the rapid development and wide application of catalysis technology, the amounts of different spent catalysts are increased from year to year.

2. Experimental

2.1. Catalyst preparation

All the catalysts were prepared by co-precipitation method. The chemicals used for research works were of analytical regent grade. A solutions of Mn-Acetate ($Mn(CH_3COO)_2.4H_2O$) was added to copper(II) nitrate ($Cu(NO_3)_2.3H_2O$) and stirred for 1 h. The mixed solution was taken in the burette and added drop wise to a solution of $KMnO_4$ under vigorous stirring conditions for co-precipitation purposes [27]. The resultant precipitate was stirred continuously for 2 h. The molar ratio of Cu/Mn in the CuMnOx catalyst was 1:8.3. Ceria was added in the form of cerium nitrate ($Ce(NO_3)_2.6H_2O$) over the $CuMn_8O_x$ at the time of precipitation process so that the ceria concentration was maintained (0.5 wt.%–3.0 wt.%) by weight in the final catalyst. The precipitate was filtered and washed several times with hot distilled water to remove all the anions. The cake thus obtained was dried at temperature 110 °C for 24 h into an oven and calcined at 300 °C for 2 h. All the precursors were calcined in three different ways; first following the traditional method of calcinations in stagnant air at 300 °C just above the decomposition temperatures of precursors for 2 h in a muffle furnace, second *in-situ* calcinations in flowing air at a rate of 32.5 ml.min^{-1} in 300 °C for 2 h. The nomenclature and calcinations strategy of catalysts was shown in Table 1. Reactive calcinations of the precursors were carried out by the introduction of low concentration of chemically reactive CO–Air mixture (4.6% CO) at a total flow rate of 32.5 ml min^{-1} over the hot precursors.

The temperature of bed was increased from room temperature to 160 °C where CO conversion has started. This temperature was maintained for a defined period of time and CO concentration was measured

Table 1
Calcinations strategy and nomenclature of the catalysts.

Catalyst name	Calcinations strategy	Nomenclature
$CuMn_8Ox$	Stagnant air calcinations	$CuMn_{8SA}$
$CuMn_8Ox$ doped Ce in fresh		$CuMn_8Ce_{FSA}$
$CuMn_8Ox$ doped Ce in Spent		$CuMn_8Ce_{SSA}$
$CuMn_8Ox$	Flowing air calcinations	$CuMn_{8FA}$
$CuMn_8Ox$ doped Ce in fresh		$CuMn_8Ce_{FFA}$
$CuMn_8Ox$ doped Ce in Spent		$CuMn_8Ce_{SFA}$
$CuMn_8Ox$	Reactive calcinations	$CuMn_{8RC}$
$CuMn_8Ox$ doped Ce in fresh		$CuMn_8Ce_{FRC}$
$CuMn_8Ox$ doped Ce in Spent		$CuMn_8Ce_{SRC}$

in the existing stream of reactor at the regular intervals until 100% CO conversion was achieved. After achieving total CO conversion the resultant catalyst was annealed for half an hour at the same temperature then the temperature was increased up to 300 °C and upheld for an hour followed by cooling to room temperature in the same environment. The nomenclature of resulting catalysts thus formed was given by the first capital letter of corresponding precursors used and the suffixes '$_{SA}$', '$_{FA}$' and '$_{RC}$' denote whether there were obtained by calcinations in air, flowing air or by RC, respectively, as presented in Table 1.

2.2. Characterization of catalysts

The Scanning electron micrographs (SEM) instrument produced the high-resolution image of catalyst by an electron beam, and the image of catalyst was recorded on a Zeiss EVO 18 (SEM) instrument. The magnification images 5000X and accelerating voltage 15 kV was applied. It provides information about the average aggregate size, crystalline degree and microstructures of catalyst. The EDX is an energy dispersive X-ray analyzer it provides information about the elemental identification and quantitative composition analysis of various compounds present in the catalyst. The X-ray diffraction (XRD) analysis of catalyst was conceded out by using Rigaku D/MAX-2400 diffractometer with Cu-Kα radiation at 40 kV and 40 mA. The mean crystallite size (d) of the catalyst was calculated from the line broadening of most intense reflection by using the Scherrer Equation [53,54]. It is a fast analytical technique, mainly applied for the measurement of phase identification, crystal orientation, crystallite size, unit cell dimensions and crystal defects, etc. The Fourier transforms infrared spectroscopy (FTIR) provides information about the kinds of materials present in catalyst by their peak values. The measurement was done by the Shimadzu 8400 FTIR spectrometer in the range of 400–4000 cm^{-1}. The Brunauer Emmett Teller Analysis (BET) provides information about the specific surface area, pore volume and pore size of the catalyst. The isotherm was recorded by Micromeritics ASAP 2020 analyzer with the physical adsorption of N_2 at the temperature of liquid nitrogen (−196 °C) with an average pressure range of 0.05–0.30 P/P_o [55,56].

2.3. Catalytic activity measurement

The conversion of CO was carried out under the following reaction conditions: 100 mg of catalyst was diluted to α-alumina with feed gas consisting of a lean mixture of (2.5 vol.% CO in air) and total flow rate was maintained at 60 mL/min. The air feed into the reactor was made free from moisture and CO_2 by passing through it CaO and KOH pellet drying towers. The catalytic experiment was carried out under the steady-state conditions and reaction temperature was raised from room temperature to 300 °C with a heating rate of 2 °C/min. The schematic diagram of experimental set up shown in Fig. 1.

To monitor the flow rate of CO and air passing through the catalyst present in reactor was analysis by the digital gas flow meters. The CO conversion was analysis by gas chromatogram to measure the activity of resulting catalyst. Pure α–alumina spheres were used in the preheating section and section after catalyst bed. Eq. (1) can be representing the air oxidation of CO over catalyst. For controlling the heating temperature of catalyst present in a reactor was done by a microprocessor-based temperature controller. The gaseous products were produced after the oxidation reaction in a reactor was analysis by an online gas chromatogram (Nucon series 5765) equipped with an FID detector, porapack q-column and a methaniser for measuring the concentration of CO and CO_2.

$$\mathbf{2CO + O_2 \rightarrow CO_2} \quad (1)$$

Where the concentration of CO was proportional to the area of chromatogram A_{CO}. The overall concentration of CO in the inlet stream was proportional to the area of CO_2 chromatogram.

$$(\mathbf{X_{CO}}) = [(\mathbf{C_{CO}})_{in} - (\mathbf{C_{CO}})_{out}]/[\mathbf{C_{CO}}]_{in} = [(\mathbf{A_{CO}})_{in} - (\mathbf{A_{CO}})_{out}]/[\mathbf{A_{CO}}]_{in} \quad (2)$$

The oxidation of CO at any instant was measured on the basis of values of the concentration of CO $(C_{CO})_{in}$ in the feed and concentration of CO_2 $(C_{CO})_{out}$ in the product stream by the following Eq. (2). Where the change in concentration of CO due to the oxidation at any instant $[(C_{Co})_{in} - (C_{Co})_{out}]$ was proportional to the area of chromatogram of CO_2 formed at that instant $[(A_{Co})_{in} - (A_{Co})_{out}]$ and concentration of CO in the inlet stream $(C_{Co})_{in}$ was proportional to the area of chromatogram of CO_2 formed $(A_{Co})_{in}$ by the oxidation of CO.

3. Catalyst characterization

Characterization of all catalysts prepared by reactive calcinations conditions was done by the following techniques and their activity for CO oxidation was discussed below.

3.1. Morphology analysis

The Scanning Electron Micrographs (SEM) instrument was applied for the microstructure analysis of various catalysts synthesis in reactive calcinations conditions. The difference in microstructure and morphology of catalysts was showed in Fig. 2. The size range of all granular particles was varied between (0.3 and 2.1 μm) calculated by "Image J software" " with varying degrees of agglomeration as mentioned in Table 2. SEM analysis clearly shows that the difference in physical microstructure of fresh and spent catalysts. In addition, smaller particle sizes and good distribution of active phases present on the catalyst surface, which causes a significant, increasing the effective surface area of catalyst [57,58].

From SEM analysis observed that the homogeneity and shape of $CuMn_8Ce_{FRC}$ catalyst particles. The addition of ceria into the $CuMn_{8RC}$ catalyst highly affects their porosity, particle size as well as the morphology of resulting catalyst. As shown in the SEM micrograph, the particles were comprised grains of coarse, fine and finest sizes resulted from using $CuMn_{8RC}$, $CuMn_8Ce_{SRC}$ and $CuMn_8Ce_{FRC}$ catalysts, respectively. The average particle size of $CuMn_{8RC}$, $CuMn_8Ce_{SRC}$ and $CuMn_8Ce_{FRC}$ catalysts were 1.985 μm, 0.396 μm and 0.345 μm, respectively. The smaller size particles present in $CuMn_8Ce_{FRC}$ catalyst has more efficient for CO oxidation on their surfaces, it results improved their catalytic activity [59,60]. The doping of CuMnOx catalyst by small amounts of Ceria was more efficient in improving the catalytic performance for CO oxidation. In the $CuMn_8Ce_{FRC}$ and $CuMn_8Ce_{SRC}$ catalyst, we have to take 2.5 wt.% Ce into the $CuMn_{8RC}$ catalyst.

The shape and homogeneity of particles have been changed with changing of various compositions present on the catalysts. The particle size in increasing order of the catalysts was as follows: $CuMn_8Ce_{FRC}$ < $CuMn_8Ce_{SRC}$ < $CuMn_{8RC}$. However, from the SEM image, few carbon filaments with a larger diameter can be observed due to the agglomerated form in spent catalyst. It is also observed that after the catalytic oxidation reaction, the size of $CuMn_8Ce_{SRC}$ catalyst was nearly same and more homogenized with carbon formed during the reaction. SEM image of spent catalyst in Fig. 2C represents that the fact that, the catalyst retained in its morphology even after reuses. SEM micrograph of spent catalyst has been shown that uniform size due to the adsorption of CO on their surfaces. The ceria doping was evenly distributed in the micrometer range over $CuMn_{8RC}$ catalyst surface regardless of the reaction temperature and improving the catalytic performance for CO oxidation. An amorphous phase was observed in the entire catalysts sample after calcinations at 300 °C temperature. The synergetic effect of catalysts depends upon the catalyst composition and nature of oxidized compounds.

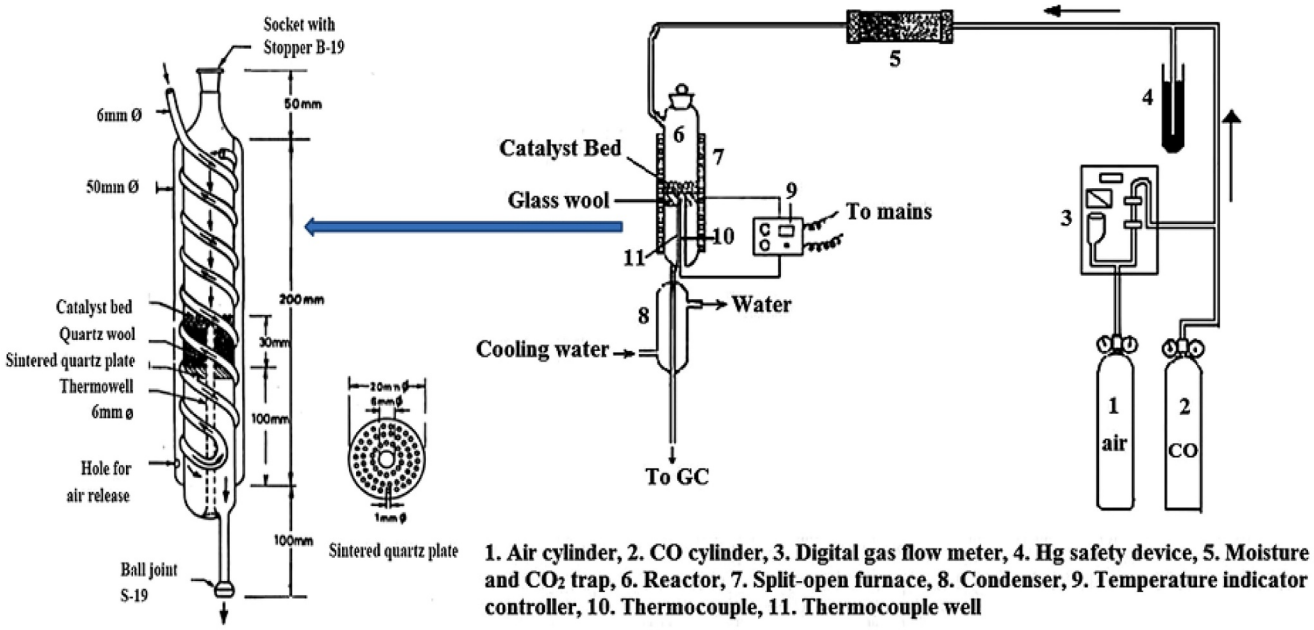

Fig. 1. Schematic diagram of experimental set up.

3.2. Elemental analysis

In order to verify the atomic percentages of various elements present in the catalysts was done by the Scanning Electron Microscopy (SEM) with Energy Dispersive X-Ray analysis (SEM-EDX) techniques. The elemental mapping was performed to determine the elemental concentration distribution of catalyst granules by using Isis 300 software as shown in Fig. 3. The result of SEM-EDX analysis has shown that all catalyst samples were pure due to the presence of their relative elemental peaks only. The doping materials associated with CuMnOx catalyst promote the oxygen storage, release and improved oxygen mobility. It was also apparent that the addition of ceria did not significantly alter the textural properties of catalysts, but the surface area was also increased. The relative atomic percentage and weight percentage of C, Cu, Mn, O and their relative doping materials species present on the surface layer of catalyst were represented in Table 3. The atomic percentage of Mn was also higher than C, Cu, Ce and O in all the catalysts.

The molar ratio of all elements present in the catalysts analysis by EDX was very close to the actual dosage of various elements present in the catalyst. The molar ratio of Cu/Mn in all the catalyst samples was approximately same as the actual dosage of Cu and Mn percentage present in the precursors. The atomic percentage of oxygen present in the catalyst was decreased in the following order: $CuMn_8Ce_{SRC}$ > $CuMn_8Ce_{FRC}$ > $CuMn_{8RC}$. The $CuMn_8Ce_{FRC}$ catalyst contained the least amount of oxygen as compared to the other catalysts.

Table 2
Particle size of catalysts.

Catalyst	Particle size (μm)
$CuMn_{8RC}$	1.985
$CuMn_8Ce_{FRC}$	0.345
$CuMn_8Ce_{SRC}$	0.396

The abundant surface oxygen atoms of $CuMn_8Ce_{RC}$ catalyst can react with absorbed CO thus lead to better catalytic activity in the Mars–van Krevelen type mechanism (MvK) which was frequently suggested for metal-oxides. The occurrence of oxygen deficiency in $CuMn_8Ce_{RC}$ catalyst has shown that the presence of high density of active sites. The carbon present in spent $CuMn_8Ce_{SRC}$ catalyst was calculated from the image J software was found in between 0.5 and 1.5 μm. The atomic and weight percentage of carbon present in the spent $CuMn_8Ce_{SRC}$ catalyst was 8.76% and 8.67%, respectively. It was

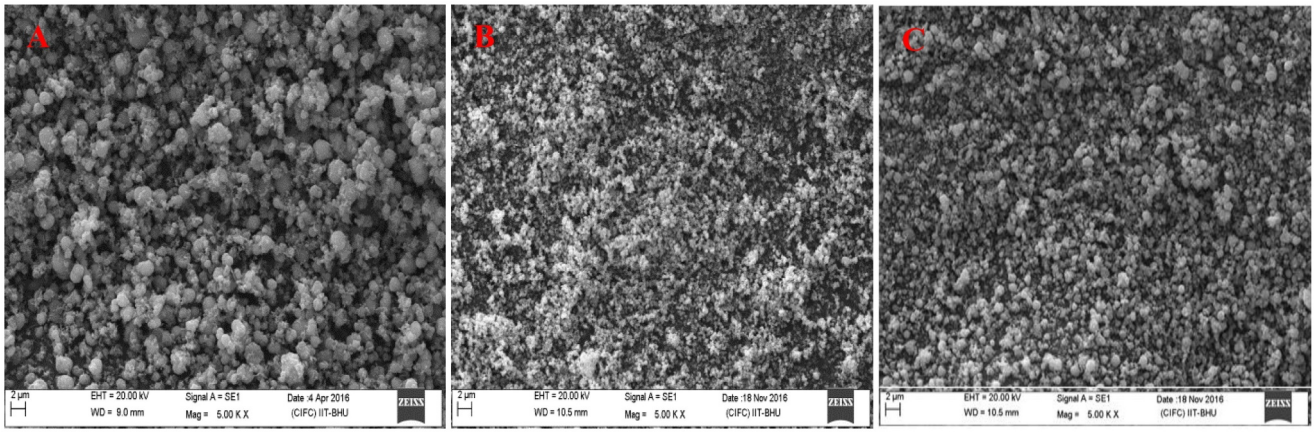

Fig. 2. SEM image of (A) $CuMn_{8RC}$, (B) $CuMn_8Ce_{FRC}$ and (C) $CuMn_8Ce_{SRC}$.

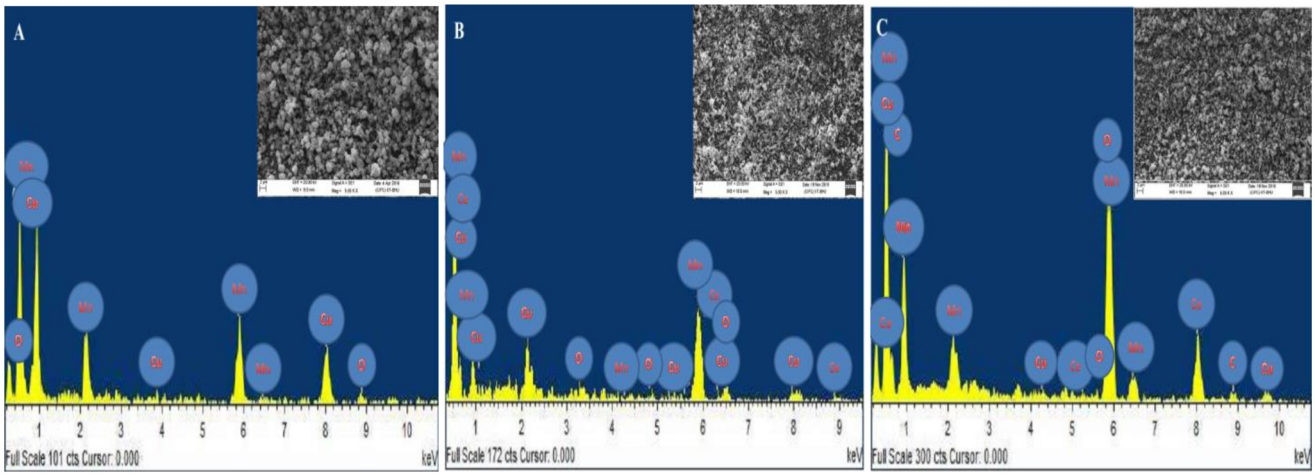

Fig. 3. SEM-EDX image of (A) $CuMn_{8RC}$, (B) $CuMn_8Ce_{FRC}$ and (C) $CuMn_8Ce_{SRC}$.

also interesting that after reaction, the percentage of Cu, Mn, Ce and O were get reduced and more homogenized with carbon formed. The presence of small amount of oxygen in the surface layer of catalyst causes the number of active sites present on catalyst surfaces has been increased [61–63].

3.3. Phase identification and cell dimensions

The phase identification and cell dimensions of catalysts prepared in reactive calcinations conditions were done by the X-ray powder diffraction (XRD) technique and displayed in Fig. 4. It provides information about the structure, phase, crystal orientation, lattice parameters, crystallite size, strain and crystal defects etc. XRD pattern of the $CuMn_{8RC}$ catalyst has shown that the diffraction peak at 2θ of 32.46 corresponds to its lattice plane (122), (121), (111), (110), (101), (133) and (221) Face-centered cubic $Cu_1Mn_8O_2$ (PDF-72-1036 JCPDS file). The crystallite size of catalyst was 3.45 nm. In reactive calcinations, prepared fresh $CuMn_8Ce_{FRC}$ catalyst has shown that the diffraction peak at 2θ of 28.65 corresponds to its lattice plane (111), (101), (133), (122), (110), (112), (211), (131), (011) and (121) of Cubic-centered $Cu_{0.5}Mn_{4.2}CeO_4$ (PDF-72-1224 JCPDS file). The crystallite size of catalyst was 2.71 nm. The XRD pattern of $CuMn_8Ce_{SRC}$ catalyst has shown that the diffraction peak at 2θ of 28.56 corresponds to its lattice plane (101), (111), (112), (110), (011), (121), (133), (221), (131) and (122) of Body-centered tetragonal $Cu_{0.6}Mn_{4.0}CeO_4$ (PDF-62-04324 JCPDS file). The crystallite size of catalyst was 2.54 nm. The broader peak in $CuMn_8Ce_{FRC}$ catalyst has shown that the relatively amorphous nature of catalyst and their structure, phase and crystallite size was also discussed in Table 4.

The crystallite size of particles present in catalyst surfaces obtained by RC conditions was as follows: $CuMn_{8RC}$ > $CuMn_8Ce_{FRC}$ > $CuMn_8Ce_{SRC.}$ It was quite apparent that the crystallite size of $CuMn_8Ce_{SRC}$ catalyst exhibited the smallest size (2.54 nm) in comparison to $CuMn_8Ce_{FRC}$ (2.71 nm) and $CuMn_{8RC}$ (3.45 nm) catalysts. From Table 4 and Fig. 4, confirmed that the particles present in $CuMn_8Ce_{FRC}$ catalyst were more crystalline form and producing narrow size high-intensity diffraction lines; as compared to other catalysts. The crystallite size of particles present in catalyst was analysis by the XRD technique was matched with their particle size calculated by the SEM characterization [64,65].

XRD analysis of spent catalyst has not found any single peak of CeO phase, whereas all of the planes of CeO_2 existed predominantly. The absence of CeO phase indicates that the reduction of CeOx into Ce during reaction or small concentration of it gets involved in carbon filament formation. The large crystallite size suggests agglomeration due to the in-situ thermal treatment process. In further experimental results prove that the lower crystallite size of $CuMn_8Ce_{FRC}$ catalyst was highly active for CO oxidation.

3.4. Identification of materials present in catalyst

The functional groups of elements are present in Ceria doped CuMnOx catalysts were done by the Fourier transforms infrared spectroscopy (FTIR) analysis. The highlighted regions show that the various types of chemical groups are present on the catalysts. The comparison spectra of different catalysts synthesize by the co-precipitation method followed by reactive calcinations conditions was shown in Fig. 5.

In the catalysts at transmittance conditions, there were total four peaks obtained, the IR band (1380 cm^{-1}) has shown that the presence of MnO_2 group, (3440 cm^{-1}) show CuO group, (1640 cm^{-1}) show CeO_2 group and (820 cm^{-1}) show CO_3^{2-} group. These bonds mainly correspond to the vibration mode of tetrahedral bonded Cu^{2+} and Mn^{2+} and octahedral coordinated Ce^{2+} ions in the $CuMn_8Ce_{RC}$ catalysts. The other phase like CO_3^{2-} was present as an impurities decrease in the following order: $CuMn_{8RC}$ > $CuMn_8Ce_{SRC}$ > $CuMn_8Ce_{FRC}$. The FTIR analysis has shown that the $CuMn_8Ce_{FRC}$ catalyst has highest purity as compared to other catalysts; therefore, get the best activity results for CO oxidation. After characterization of spent $CuMn_8Ce_{SRC}$ catalyst observe that the presence of (C+ $CuMn_8Ce_{FRC}$) group in the catalyst. After FTIR analysis confirm that the Cu, Mn and Ce present in $CuMn_8Ce_{FRC}$ catalyst was in the form of CuO, MnO_2 and CeO_2, respectively.

Table 3
The atomic and weight percentage of catalysts.

Catalyst	Atomic percentage (%)					Weight percentage (%)				
	C	Cu	Mn	Ce	O	C	Cu	Mn	Ce	O
$CuMn_{8RC}$	–	13.15	81.29	–	5.56	–	13.23	81.14	–	5.63
$CuMn_8Ce_{FRC}$	–	12.45	80.56	2.45	4.54	–	12.38	80.48	2.48	4.66
$CuMn_8Ce_{SRC}$	8.76	10.38	74.34	2.24	4.28	8.67	10.44	74.26	2.32	4.31

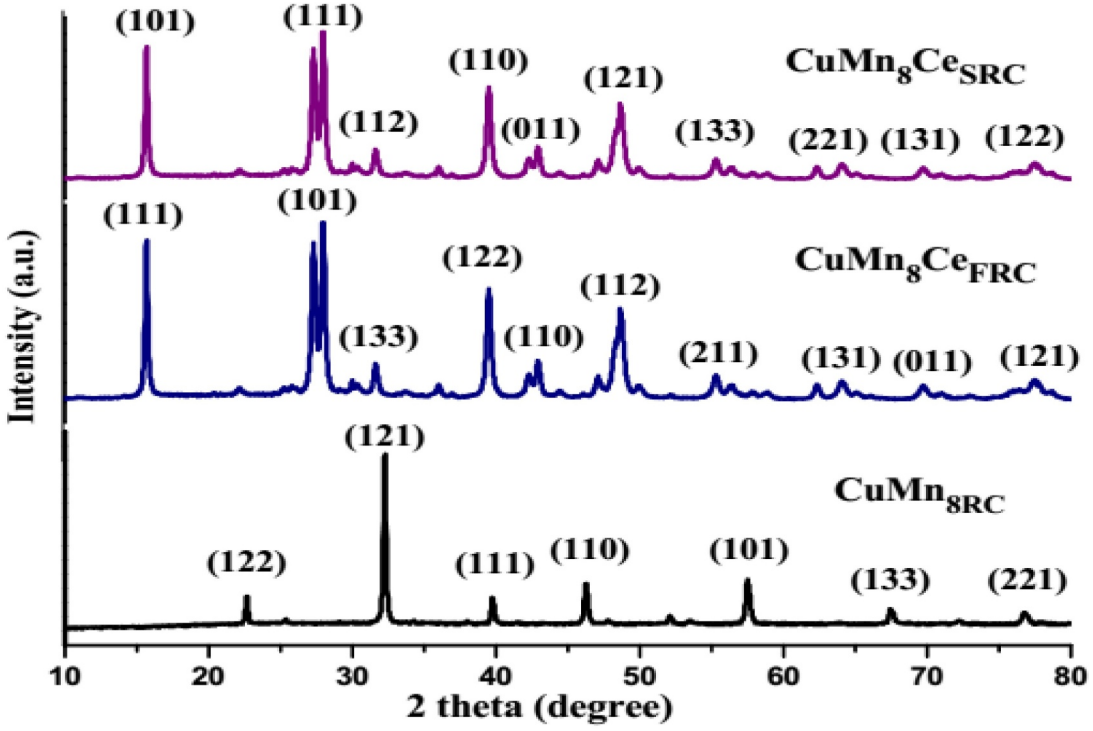

Fig. 4. XRD analysis of catalysts.

Table 4
XRD analysis of the catalysts.

Catalyst	Structure	Phase	Crystallite size
$CuMn_{8RC}$	Face-centered cubic	$Cu_1Mn_8O_2$	3.45 nm
$CuMn_8Ce_{FRC}$	Cubic-centered	$Cu_{0.5}Mn_{4.2}CeO_4$	2.71 nm
$CuMn_8Ce_{SRC}$	Body-centered tetragonal	$Cu_{0.6}Mn_{4.0}CeO_4$	2.54 nm

3.5. Identification and quantification of elements

The elemental composition and surface valance state of catalysts was characterized by XPS analysis. It was mainly used to recognize the physical and chemical change of catalyst by exposure of gaseous molecules under different thermal conditions has been examined. The high binding energy was preferably for CO oxidation. The XPS spectra in Cu

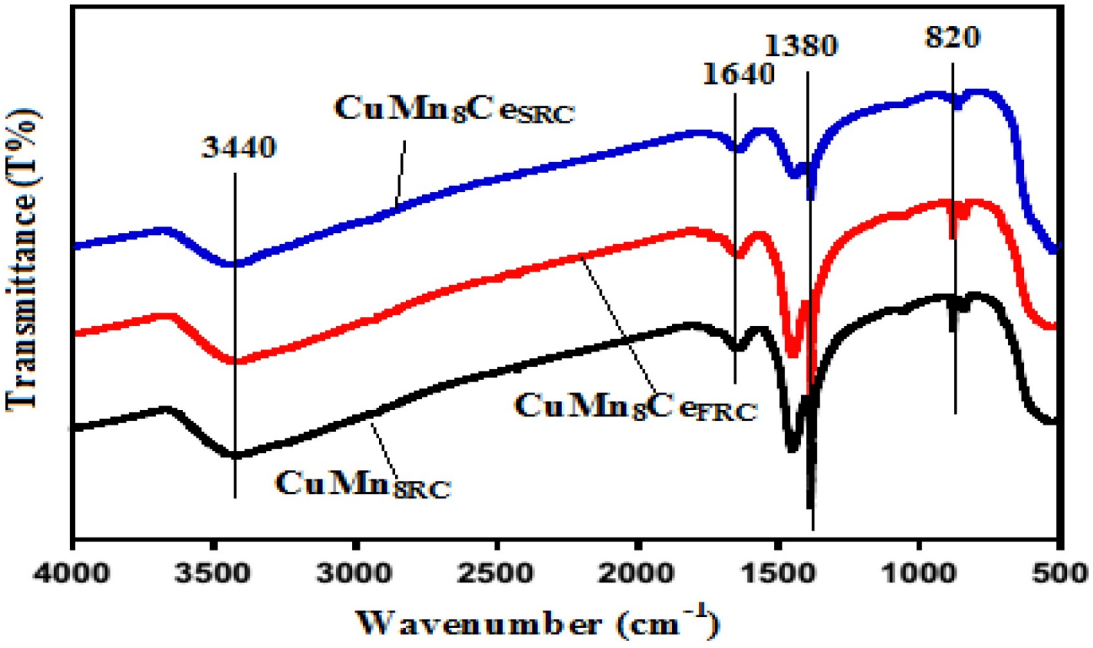

Fig. 5. FTIR analysis of doped and undoped CuMnOx catalysts.

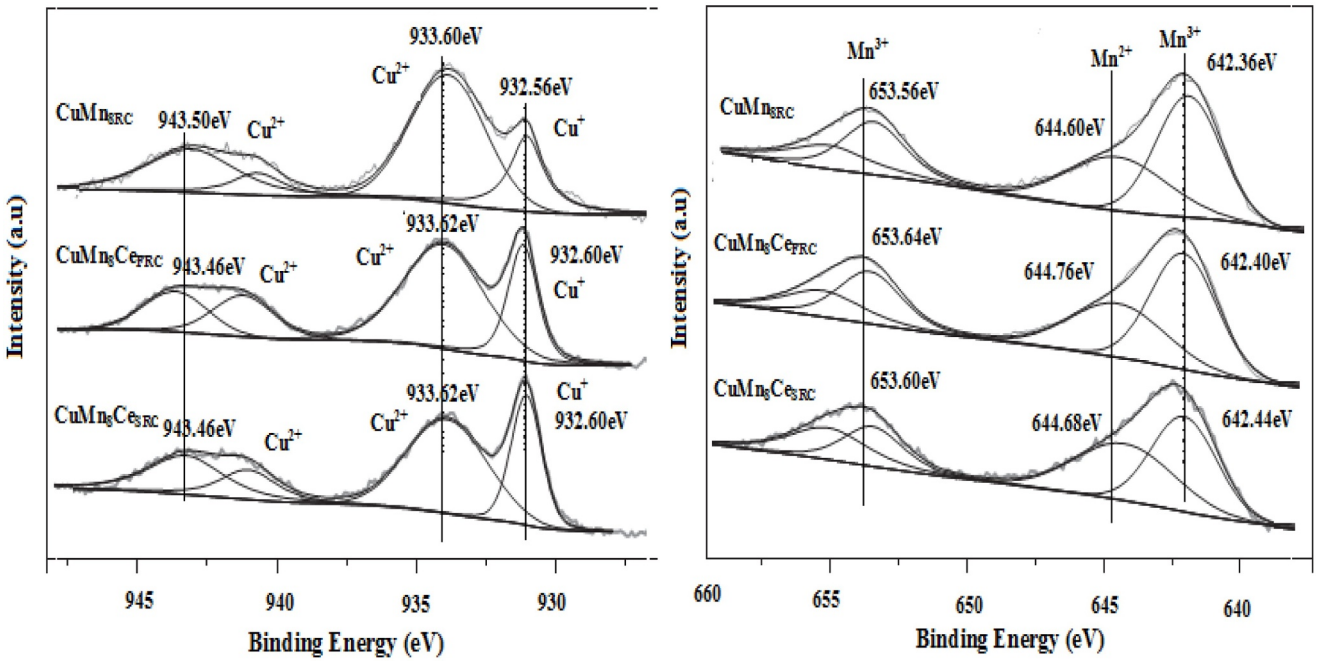

Fig. 6. XPS spectra of Cu(2p) and Mn(2p) in all catalysts.

Table 5
Binding energy and chemical state of catalysts.

Sample	Elements Cu	Mn	Ce	O
$CuMn_{8RC}$	Cu(II) Oxide 943.50eV	MnO_2 653.56eV	—	C-O 532.16 eV
$CuMn_8Ce_{FRC}$	Cu(II) Oxide 943.46eV	MnO_2 653.64eV	CeO_2 916.45eV	C-O 531.56 eV
$CuMn_8Ce_{SRC}$	Cu(II) Oxide 943.46eV	MnO_2 653.60eV	CeO_2 916.30eV	C-O 532.04 eV

(2p), Mn(2p), Ce(2p) and O(1 s) regions are shown in the figure. The prominent peak of Cu(2p) level in $CuMn_{8RC}$, $CuMn_8Ce_{FRC}$ and $CuMn_8Ce_{SRC}$ catalysts were deconvoluted into three peaks centered as shown in Fig. 6. The binding energy of Cu(2p) in $CuMn_{8RC}$ catalyst was 943.50 eV, 933.60 eV and 932.56 eV and highest binding energy peak of Cu(2p) in $CuMn_{8RC}$ catalyst was obtained at 943.50 eV. In $CuMn_8Ce_{FRC}$ catalyst Cu(2p) peak was 943.46 eV, 933.62 eV and 932.60 eV and highest binding energy peak was obtained at 943.46 eV. The binding energy peak of Cu(2p) in $CuMn_8Ce_{FRC}$ and $CuMn_8Ce_{SRC}$ catalyst was almost same. By performing peak fitting deconvolution of main Cu(2p) in all the calcinations catalyst was obtained at Cu(II) oxide form. From Table 5 and Fig. 6 confirm that the binding energy peak of Cu(2p) in $CuMn_8Ce_{FRC}$ and $CuMn_8Ce_{SRC}$ catalyst was highest as comparison to $CuMn_{8RC}$ catalyst. By performing peak fitting deconvolution of prominent peak of Mn(2p) level in all catalysts was deconvoluted into double peaks centered as shown in Fig. 6. There were two main components including Mn^{2+} and Mn^{3+} present in all the catalysts and difference between the binding energy values were small. The binding energy of Mn(2p) in $CuMn_{8RC}$, $CuMn_8Ce_{FRC}$ and $CuMn_8Ce_{SRC}$ catalysts were (642.36 eV, 644.60 eV and 653.56 eV), (642.40 eV, 644.76 eV and 653.64 eV) and (642.44 eV, 644.68 eV and 653.60 eV), respectively, and associated with the presence of Mn^{2+} and Mn^{3+} in all the catalysts. The highest binding energy peak of Mn(2p) in $CuMn_{8RC}$, $CuMn_8Ce_{FRC}$ and $CuMn_8Ce_{SRC}$ catalysts were 653.56 eV, 653.64 eV and 653.60 eV, respectively. The peak fitting deconvolution of Mn(2p) exist in all catalysts was MnO_2 form. The prominent peak of Ce(3d) level in $CuMn_8Ce_{FRC}$ and $CuMn_8Ce_{SRC}$ catalysts were deconvoluted into six peaks centered as shown in Fig. 7. The highest binding energy peak of Mn(2p) in $CuMn_{8RC}$, $CuMn_8Ce_{FRC}$ and $CuMn_8Ce_{SRC}$ catalysts were 653.56 eV, 653.64 eV and 653.60 eV, respectively. The peak fitting deconvolution of Mn(2p) in all catalysts was MnO_2 form.

The prominent peak of Ce(3d) level in $CuMn_8Ce_{FRC}$ and $CuMn_8Ce_{SRC}$ catalyst was deconvoluted into six peaks centered as shown in Fig. 7. The binding energy peak of Ce(3d) in $CuMn_8Ce_{FRC}$ catalyst was 916.45 eV, 908.60 eV, 902.40 eV, 885.40 eV, 890.60 eV and 883.60 eV and $CuMn_8$ Ce_{SRC} catalyst was 916.30 eV, 908.54 eV, 902.36 eV, 885.32 eV, 890.46 eV and 883.56 eV. The highest binding energy peak of $CuMn_8Ce_{FRC}$ and $CuMn_8Ce_{SRC}$ catalysts were 916.45 eV and 916.30 eV, respectively. The absolute distinctions between Ce^{3+} and Ce^{4+} could not be resolved due to the complex electronic structure. The presence of Ce^{3+} was assigned to the generation of oxygen vacancy according to the charge compensation. The surface relative Ce^{3+}/Ce^{4+} molar ratio was calculated from the normalized peak areas of Ce^{4+} and Ce^{3+} core level spectra. This result was also in good agreement with the fact that Ce^{3+} has a larger effective ionic radius than that of Ce^{4+}, thus the increase of Ce^{3+} would result in an expansion of CeO_2 lattice. In the present study, the oxygen with binding energy of 531.46 eV and 532.16 eV was main form and could be assigned to the chemisorbed oxygen (Oa). One of noticeable fact was that the amount of oxygen presents less in reactive calcined prepared $CuMn_8Ce_{FRC}$ catalyst as compared to the $CuMn_{8RC}$ and $CuMn_8Ce_{SRC}$ catalysts, due to the absence of lattice oxygen which can creates oxygen vacancies for CO oxidation. Thus, it was well known that the defects/dislocations were improved the active sites for CO oxidation reaction.

The increasing ratio of $O_{ads}/(O_{ads}+O_{lat})$ was desirable for producing highly active catalysts and ratio of all catalysts was as follows: $CuMn_8Ce_{FRC}$ > $CuMn_8Ce_{SRC}$ > $CuMn_{8RC}$. The XPS data suggested that all catalysts were pure and there will be no impurities were present in the catalyst. Finally observed that the high binding energy peak of Cu (2p), Mn(2p), Ce(3d) and O(1 s) present in the $CuMn_8Ce$ catalyst was much better for fresh catalyst as compared to the spent catalyst. For relatively lower Ce loading, small agglomerates of (more or less doped) ceria nanoparticles of very small size highly dispersed over the $CuMn_{8RC}$ catalyst support and interfacial sites of support constitute relatively minor portion of surface exposed centers of this component. The Cu^+ cations have been proposed to appear in the $CuMn_{8RC}$ catalyst as a consequence of redox equilibrium between Cu^{2+}/Cu^+ and $Mn^{3+}/$

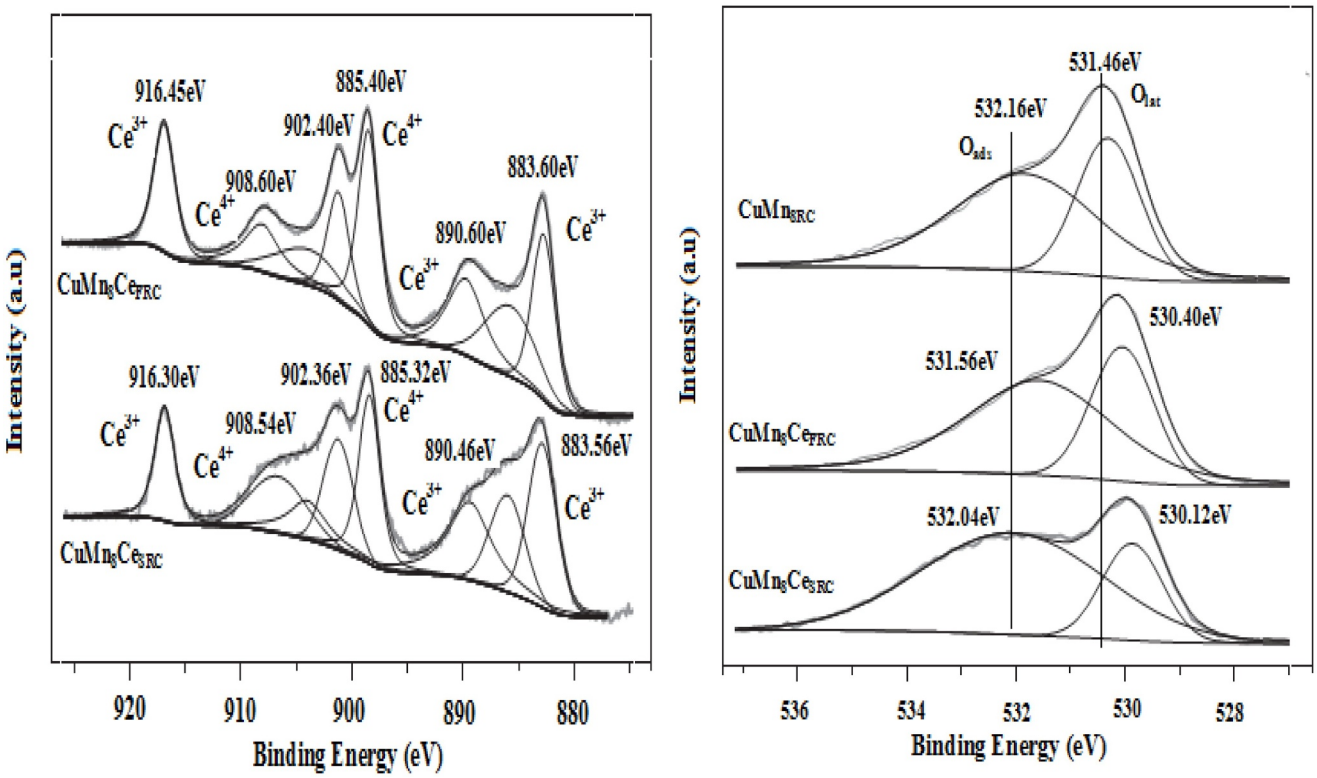

Fig. 7. XPS spectra of Ce(3d) and O(1 s) in all catalysts.

Mn^{4+} in an amount which depends on the temperature of thermal treatment employed for its preparation.

However, the gradual decrease observed in Cu^{+} contribution upon increasing the Ce loading was not accompanied by simultaneous decrease of Mn^{4+} component. The XPS results showed that the Cu^{+} decrease could be related to the interaction of support with Ce, which could favor for transfer of electrons from Cu^{+} sites to the Ce nanoparticles [45–46].

3.6. Surface area measurement of catalyst

The surface areas of Ceria doped CuMnOx catalysts were synthesized into the laboratory by co-precipitation method followed by reactive calcinations conditions was analysis by the BET technique. The isotherm curves of different catalysts showing that the hysteresis loops of which desorption branch joined the adsorption curve with relative

Table 6
Textural property of catalysts.

Catalyst	Surface Area (m^2/g)	Pore Volume(cm^3/g)	Ave. Pore Size (Å)
$CuMn_{8RC}$	86.28	0.534	63.2
$CuMn_8Ce_{SRC}$	113.36	0.542	54.2
$CuMn_8Ce_{FRC}$	124.38	0.624	48.6

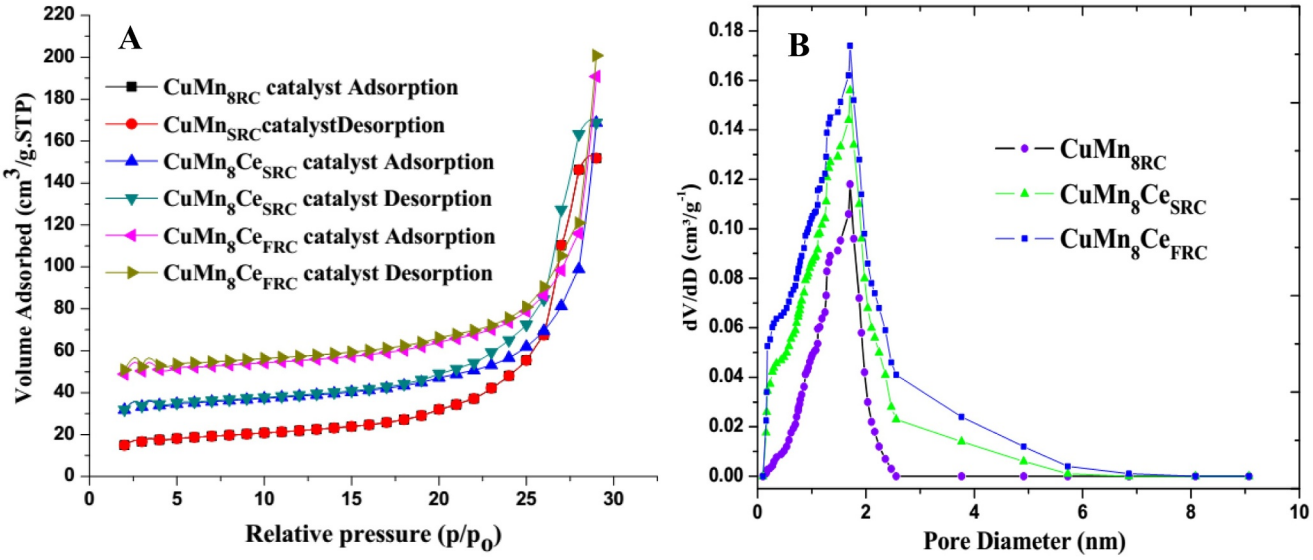

Fig. 8. Textural properties (A) N_2 adsorption-desorption isotherms and (B) Pore size distributions.

pressure 0.7 were displayed in Fig. 8 and Table 6. The catalyst samples exhibited a hysteresis loop, which indicated that the pores were exhibiting geometries of mesopores. The mesopores geometries of synthesized catalysts exhibited H1 hysteresis loops. The pore size distributions (PSDs) as measured by the Barrett–Joyner–Halendar (BJH) method from the desorption branch of nitrogen isotherms [47]. The presence of hysteresis loop at a relative pressure (P/P_0) of 0.8–1.0 indicates that the porosity arising from non-crystalline intra-aggregate voids and spaces formed by the inter-particle contacts. Fig. 8(A) shows that the N_2 adsorption-desorption isotherms and pore size distributions of $CuMn_{8RC}$, $CuMn_8Ce_{FRC}$ and $CuMn_8Ce_{SRC}$ catalysts, respectively. The surface area of $CuMn_{8RC}$, $CuMn_8Ce_{FRC}$ and $CuMn_8Ce_{SRC}$ catalysts were 86.28, 124.38 and 113.36 m^2/g, respectively. The specific surface area and total pore volume were two major factors which can affects the catalytic activity for CO oxidation. The isotherm gave useful information on the mesopores structure through its hysteresis loop. The surface area and pore volume of catalyts are also represents in Table 6.

The order of surface area of catalysts was as follows: $CuMn_8Ce_{FRC}$ > $CuMn_8Ce_{SRC}$ > $CuMn_{8RC}$. The surface area, pore volume and pore size of $CuMn_8Ce_{FRC}$ catalyst were very much superior to the $CuMn_8Ce_{SRC}$ and $CuMn_{8RC}$ catalysts. A large number of more pores present in $CuMn_8Ce_{FRC}$ catalyst have a huge number of CO molecules chemisorbed on the catalyst surfaces, therefore shows that the better catalytic activity. The specific surface area was measured by BET analysis and also followed by the SEM and XRD results.

On the basis of gaseous products formed during the reaction, the most probable reaction to produce carbon can be considered either conversion of CO into CO_2. During the reaction between catalyst and CO, the number of pores present in catalyst surfaces was blocked therefore the surface area of spent catalyst was decreases. The textural property obtained for spent catalysts shows a strong change in the number of active sites. The differences between weight losses obtained for fresh and spent catalyst was observed at high temperature. From the characterization results observed that the textural property like surface area, morphology, binding energy, pore volume, pore size, chemical state of spent catalyst was slightly decreasing than the fresh catalyst [66,67].

3.7. Particle size and morphology analysis

TEM investigations were carried out to recognize the particle size and morphology of prepared catalyst samples. Selected area electron diffraction (SAED) patterns (insets) represents that the $CuMn_{8RC}$ and $CuMn_8Ce_{RC}$ catalysts were amorphous in nature due to the lack of diffraction rings or spot patterns, in agreement with the XRD result. The TEM analysis also confirms that presence of catalytic active sites as $CuMn_8Ce_{SRC}$ spent catalyst. For comparison, TEM image of spent $CuMn_8Ce_{SRC}$ and fresh $CuMn_8Ce_{FRC}$ catalysts at 100 nm was shown in Fig. 9. The fresh catalyst showed a multilayer (3–4) staking of $CuMn_8Ce_{FRC}$ with an average length of 12.2 nm, while multilayer of $CuMn_8Ce_{SRC}$ stacking was not seen for spent catalyst as well as the length of layer was about 3.12 nm, which were agglomerated carbon deposition on the catalyst surface or remain as a single crystal (Single slab). The spent catalyst showed relatively stumpy $CuMn_8Ce_{SRC}$ stacking, which indicated that the deposited species deform the $CuMn_8Ce_{RC}$ stacking or catalytic active sites. The TEM images were shown in Fig. 9 represents that the grain size of $CuMn_{8RC}$ was 15 nm. The block units for each catalyst were nanoparticles of 5–15 nm in size and some hierarchical microstructures including spheres, spindles and dumbbells were formed [67–70].

As the Mn ions were smaller than the Ce ions, the replacement of Mn ions at the Ce sites will shrink the lattice and detected by the TEM image. The Ce has a cubic fluorite-type structure and lattice parameter of pristine Ce was around 0.534 nm. The manganese species in the mixed oxides showed a spectrum of MnO_2 and different from that of CeO_2, indicating that the majority of manganese oxides present in the form of MnO_2, regardless as highly dispersed clusters in the fresh catalyst and sintered crystallites in the aged catalyst. Ceria has also influenced the oxidation states of manganese. Compared with the dominating MnO_2 state in pure manganese oxide by the same synthesis, the manganese in ceria lattice presents mainly in the Mn^{3+} states and exhibited a facile redox behavior [71,72]. A clean surface of $CuMn_8Ce_{FRC}$ catalyst exposed by a mixture of CO and air quickly becomes covered with CO since CO requires a single vacant adsorption site in the spent $CuMn_8Ce_{SRC}$ catalyst. Catalyst sintering was significant as a major difference in $CuMn_8Ce_{RC}$ crystallite size was also observed in the TEM images of fresh and spent catalysts, indicating that the catalyst deactivation occurred mainly due to the deposition of carbonaceous species.

Moreover, amorphous carbon was found in the TEM micrograms of deposited carbon on the $CuMn_8Ce_{RC}$ catalyst's surface. The TEM image provides insight into the microstructure details of nano-particles of all catalysts. The average particle diameter of fresh $CuMn_8Ce_{FRC}$ catalyst was 4–7.5 nm and spent $CuMn_8Ce_{SRC}$ catalyst was found to be 3–4.5 nm. In Fig. 10(C), the carbon filaments were bonded to the Cu-Mn-Ce particles at the top with the unblocked surface, their formation not necessarily causes catalyst deactivation. However, ceria crystallites on the top of filamentous carbon lose their contact with the Cu-Mn particle, so that the course of catalytic reaction can be changed. The loss of activity in $CuMn_8Ce_{RC}$ catalyst was mainly caused by the kind of carbon which encapsulates catalyst surface after the CO oxidation reaction [73–75].

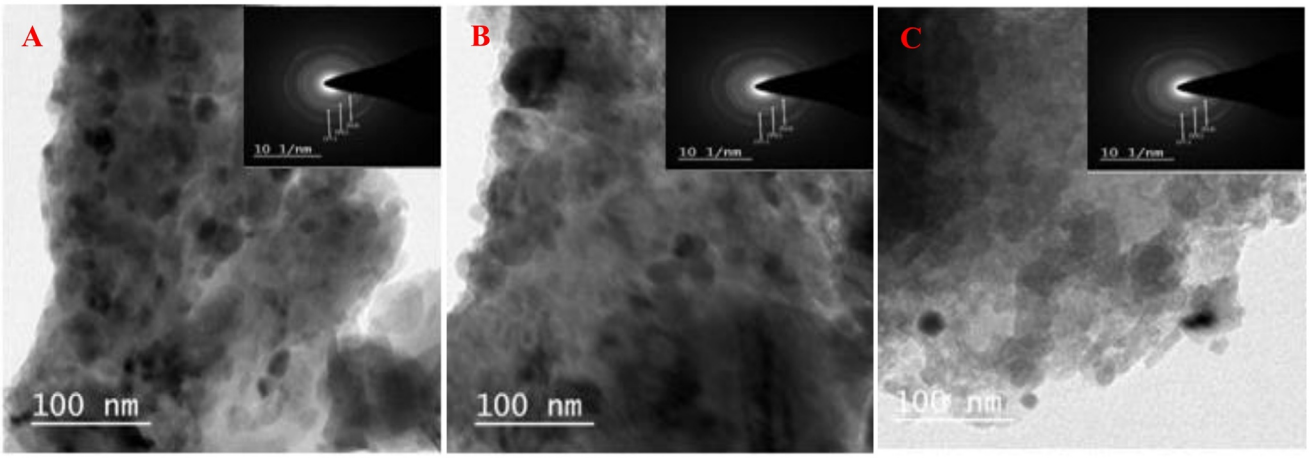

Fig. 9. TEM image of (A) $CuMn_{8RC}$, (B) $CuMn_8Ce_{FRC}$ and (C) $CuMn_8Ce_{SRC}$ catalyst.

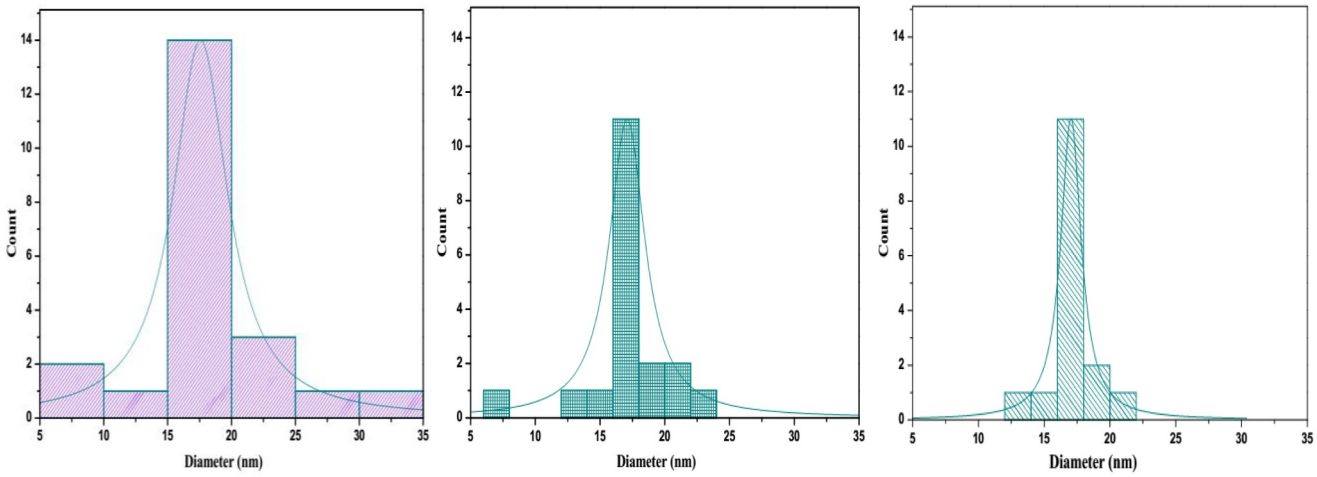

Fig. 10. Particle size of (A) $CuMn_{8RC}$, (B) $CuMn_8Ce_{FRC}$ and (C) $CuMn_8Ce_{SRC}$ catalyst.

4. Catalyst performance and activity measurement

Activity measurement of catalyst was carried out to evaluate the efficiency of resulting catalysts as a function of temperature. It was measured in different calcination conditions like stagnant air, flowing air and reactive calcination conditions. The activity was increased with the increase of temperature from room temperature ~25 °C to a certain high temperature for full conversion of CO. The light-off characteristics were used to evaluate the activity of resulting catalysts with the increasing of temperature. The characteristic temperature T_{10}, T_{50} and T_{100} corresponds to the initiation of oxidation, 50% conversion and full conversion of CO, respectively.

4.1. Blank experiment

A blank experiment was carried out with Al_2O_3 only in the place of catalyst. The bed temperature was increased up to 300 °C, practically no oxidation of CO has been observed under the experimental conditions. The blank test shows that the performance of reactor in the absence of catalyst for CO oxidation with the increasing of temperature does not show any activity for CO oxidation. Thus, the catalytic effect of reactor wall and alumina use as diluents can be neglected within the experimental conditions.

4.2. Activity measurements of catalysts at traditional calcination conditions

An activity measurement of catalysts was done into the laboratory at stagnant air calcinations (SAC) conditions for CO oxidation purposes. The stagnant air calcinations of different precursors were done in muffle furnace at the presence of stagnant air. A combination of factors including preparation conditions, calcinations strategy and various elements presence on the catalyst surfaces was highly influenced on the catalytic activity. The oxidation of CO was initiated in SAC at 35 °C over $CuMn_8Ce_{FSA}$ catalyst, which was lower by 35 °C over than that of $CuMn_{8SA}$ catalyst and half conversion of CO over $CuMn_8Ce_{FSA}$ catalyst was 80 °C, which was less by 40 °C over than that of $CuMn_{8SA}$ catalyst. The complete conversion of CO was achieved at135 °C over $CuMn_8Ce_{FSA}$, which was lowered by 20 °C, over than that of $CuMn_{8SA}$ catalyst.

In the initial conditions, a very slow exothermic reaction for CO oxidation was going on over the catalyst, it causes rising in the local temperature as discussed in Table 7 and Fig. 11. In flowing air calcination conditions the oxidation of CO was initiated at 25 °C over $CuMn_8Ce_{FFA}$ catalyst, which was lower by 5 °C over than that of $CuMn_{8FA}$ catalyst and half conversion of CO over $CuMn_8Ce_{FFA}$ catalyst was 50 °C, which was lower by 20 °C over than that of $CuMn_{8FA}$ catalyst. The complete conversion of CO was achieved at 95 °C over $CuMn_8Ce_{FFA}$, which was lower by 25 °C, over than that of $CuMn_{8FA}$ catalyst. An activity of catalysts seems to be dominated both by their average oxidation numbers and presence of different species in the catalyst surfaces [48]. An activity of catalyst prepared in FAC was shown in Fig. 11(B) and Table 7.

Table 7
Light-off characteristics of catalysts obtained by stagnant air and flowing air calcinations conditions.

Characteristics Temp.	Stagnant air		Flowing air	
	$CuMn_{8SA}$	$CuMn_8Ce_{FSA}$	$CuMn_{8FA}$	$CuMn_8Ce_{FFA}$
T_{10} (°C)	70	35	30	25
T_{50} (°C)	120	80	70	50
T_{100} (°C)	155	135	120	95

An activity order of catalysts for CO oxidation was as follows: $CuMn_8Ce$ > $CuMn_8$. After the activity test observed that the $CuMn_8Ce$ catalyst has a higher catalytic activity for CO oxidation at a lower temperature. As compared to stagnant air calcinations, the flowing air produced more active catalysts for CO oxidation at a low temperature. The order of activity for various calcinations conditions was as follows: FAC > SAC. The activity order of each catalyst for complete oxidation of CO was in accordance with their characterization [49,50].

4.3. Synthesis of catalysts by reactive calcination conditions

The reactive calcination process minimized a process step by converting two steps processes into single step process in a reactive CO-air mixture at a 300 °C temperature. The oxidation of CO was initiated in reactive calcinations conditions at 25 °C over $CuMn_8Ce_{FRC}$, which was lowered by 3 °C over than that of $CuMn_{8RC}$ catalyst and half conversion of CO over the $CuMn_8Ce_{FRC}$ catalyst was 45 °C which was lower by 5 °C over than that of $CuMn_{8RC}$ catalyst. The complete conversion of CO was achieved at 65 °C over $CuMn_8Ce_{FRC}$ catalyst, which was lower by 20 °C over $CuMn_{8RC}$ catalyst, respectively. The $CuMn_8Ce_{FRC}$ catalyst has shown that the best catalytic activity towards CO oxidation at a low temperature as shown in Table 8 and Fig. 12.

An activity order of catalysts synthesized in RC conditions for CO oxidation was as follows: $CuMn_8Ce_{FRC}$ > $CuMn_{8RC}$. The order of activity for various calcinations conditions was as follows: RC > FAC > SAC. The $CuMn_8Ce_{FRC}$ catalyst has shown that the best performance for CO oxidation at a low temperature and these systems were now worthy for further investigation.

The decrease in catalytic activity was highly reversible and appears

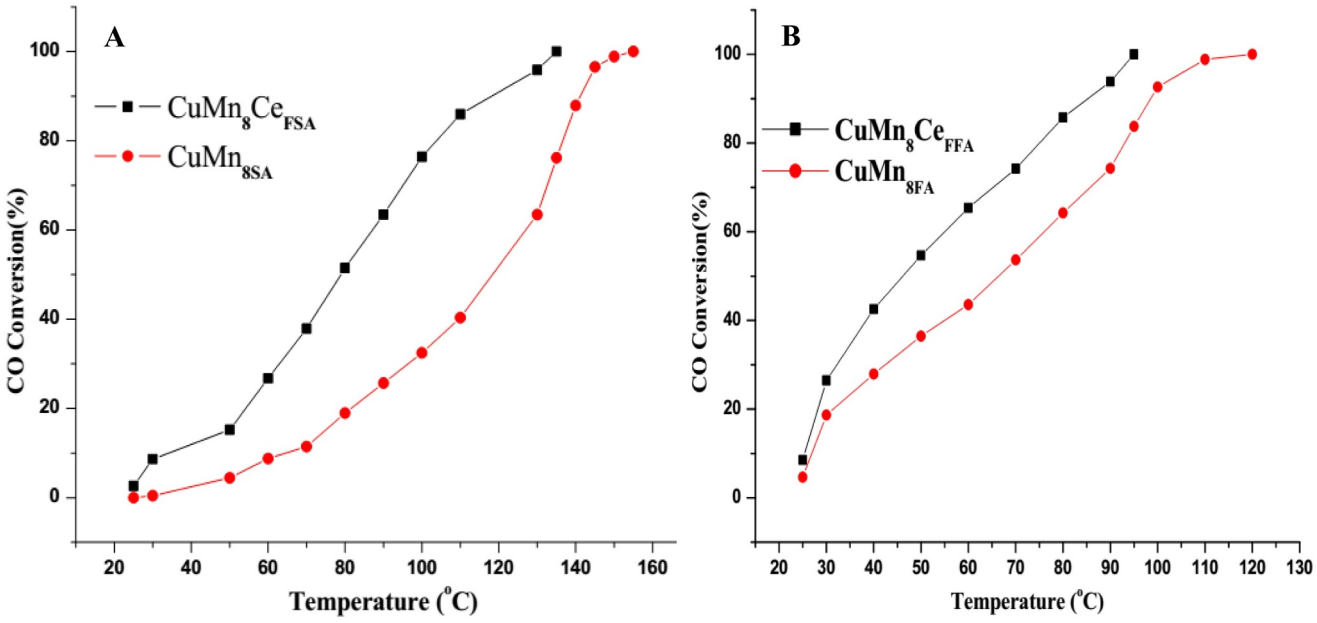

Fig. 11. Activity test of catalysts in (A) Stagnant air and (B) Flowing air calcinations.

Table 8
Light-off characteristics of catalysts in RC.

Catalyst	T_{10}	T_{50}	T_{100}
$CuMn_{8RC}$	28 °C	50 °C	85 °C
$CuMn_8Ce_{FRC}$	25 °C	45 °C	65 °C

to be primarily due to the physical blocking of catalyst surface and prevention adsorption of CO and/or O_2 under the reaction conditions. The presence of uniform pore size distribution over $CuMn_8Ce_{FRC}$ catalyst was key factor in improving their catalytic performance [51,52].

4.4. Comparison of reactive calcinations with traditional calcinations

The RC route was the most appropriated calcinations strategy for production of highly active $CuMn_8Ce_F$ catalyst for CO oxidation. A comparative study of CO oxidation over ($CuMn_8$ Ce_{FSA}, $CuMn_8Ce_{FFA}$ and $CuMn_8Ce_{FRC}$) catalysts produced under the various calcinations conditions of stagnant air, flowing air and reactive calcinations condition have shown in Fig. 13 and discussed in Table 9. The calcinations strategies have a drastic effect on the activity of resulting catalyst. The oxidation of CO was initiated in reactive calcinations conditions at 25 °C over $CuMn_8Ce_{FRC}$ catalyst, which was lowered by 3 °C and 5 °C

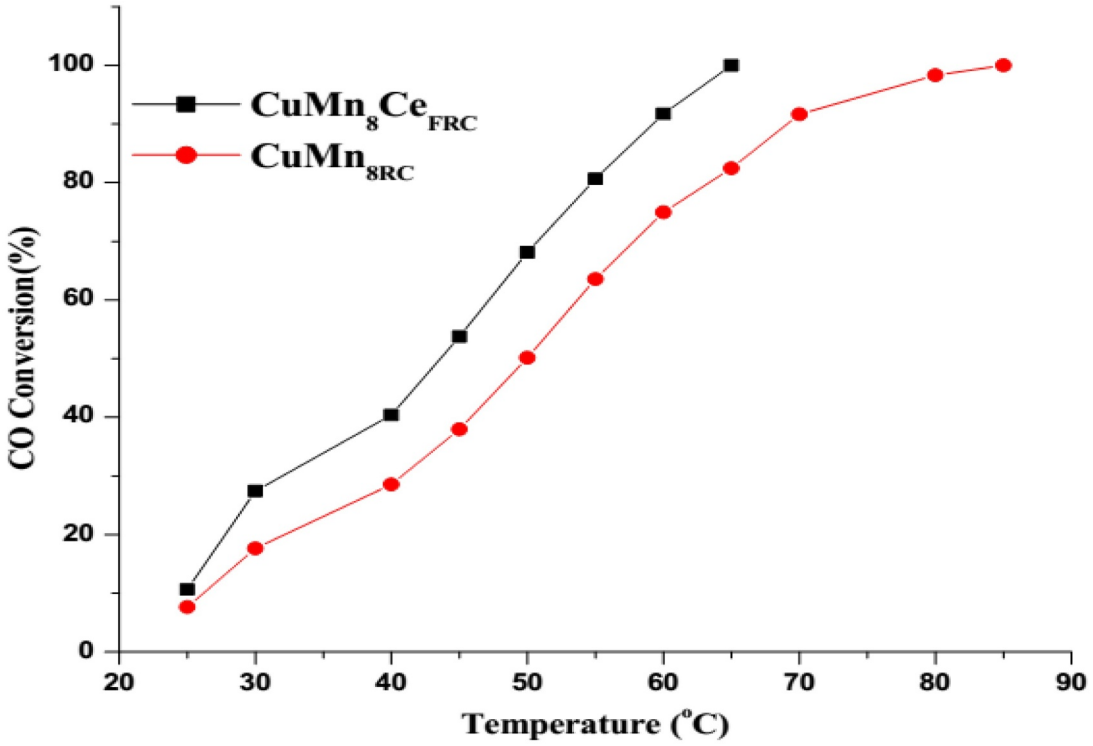

Fig. 12. Conversion of CO over various catalysts at reactive calcinations conditions.

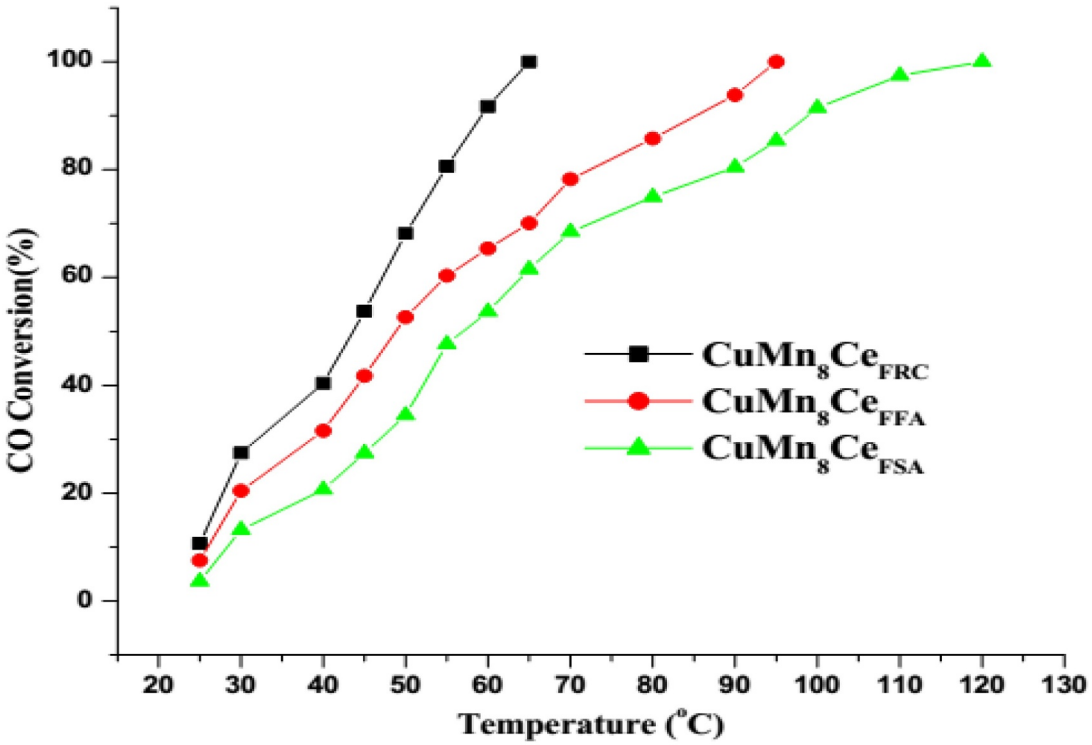

Fig. 13. Activity test of $CuMn_8Ce_F$ catalysts under various calcinations conditions.

Table 9
Light-off characteristics of $CuMn_8Ce_F$ catalysts.

Catalyst	T_{10}	T_{50}	T_{100}
$CuMn_8Ce_{FRC}$	25 ºC	45 ºC	65 ºC
$CuMn_8Ce_{FFA}$	28 ºC	50 ºC	95 ºC
$CuMn_8Ce_{FSA}$	30 ºC	60 ºC	120 ºC

over than that of $CuMn_8Ce_{FFA}$ and $CuMn_8Ce_{FSA}$ catalyst, respectively, and half conversion of CO over the $CuMn_8Ce_{FRC}$ catalyst was 45 ˚C, which was lower by 5 ˚C and 15 ˚C over than that of $CuMn_8Ce_{FFA}$ and $CuMn_8Ce_{FSA}$ catalyst, respectively. The complete conversion of CO has occurred at 65ºC over $CuMn_8Ce_{FRC}$ catalyst, which was lower by 30 ˚C and 55 ˚C over than that of $CuMn_8Ce_{FFA}$ and $CuMn_8Ce_{FSA}$ catalysts, respectively.

The activity order for CO oxidation in the decreasing sequence was in accordance with their characterization by SEM-EDX, BET, XRD, XPS and FTIR as follows: $CuMn_8Ce_{FRC}$ > $CuMn_8Ce_{FFA}$ > $CuMn_8Ce_{FSA}$. The improved catalytic activity of RC can be described to the unique structural and textural characteristics such as the smallest crystallites of $CuMn_8Ce_{FRC}$ catalyst [51].

The highest activity of $CuMn_8Ce_{FRC}$ catalyst was associated with the formation of smallest crystallites authenticated by XRD observation. The highly dispersed and specific surface area could expose more active sites for catalytic oxidation and relatively open-textured pores which will favor for the adsorption of reactants and desorption of products and thus facilitate the oxidation process. The presence of partially reduced phase provides an oxygen deficient defective structure which can creates high density of active sites as a result of reactive calcinations, consequently $CuMn_8Ce_{FRC}$ turns into the most active catalyst.

4.5. Optimization of ceria doping in $CuMn_{8RC}$ catalyst

The catalytic activity of Ce doped $CuMn_{8RC}$ catalyst was also depends upon the ceria loading (wt.%). The overall activity for CO oxidation was increased as the Ceria loading percentage increase from 1 to 2.5 wt%, then slightly decrease with a further increase in loading up to 3wt%. The activity test of doped and un-doped Ceria loading $CuMn_{8RC}$ catalysts was performed at 65 ˚C temperature as shown in Fig. 14 and described in Table 10. The trend of activity over catalysts was in accordance with XRD, BET, TEM and SEM results emphasizing that the smaller crystallite size, as well as particle size, higher surface area and easy reducibility, produce an efficient catalyst for CO oxidation. The conversion of CO at fixed temperature 65 ˚C over $CuMn_{8RC}$, 0.5%Ce-$CuMn_8Ox_{FRC}$, 1.0%$CeCuMn_8Ox_{FRC}$, 1.5%$CeCuMn_8Ox_{FRC}$, 2.0%Ce-$CuMn_8Ox_{FRC}$, 2.5%$CeCuMn_8Ox_{FRC}$ and 3.0%$CeCuMn_8Ox_{FRC}$ was 61.54%, 72.30%, 85.75%, 92.45%, 98.75%, 100% and 99.35%, respectively. The optimization of ceria loading in CuMnOx catalysts as described in Table 10.

The modification of $CuMn_{8RC}$ with ceria caused the incorporation of ceria ions into the $CuMn_{8RC}$ catalysts lattice leading to the expansion of cell volume and inhibition of crystallites growth corresponding to increase of the specific surface area of $CeCuMn_8Ox_{FRC}$ catalysts. The superior CO oxidation catalytic activity over $CeCuMn_8Ox_{FRC}$ catalyst in the air was attributed to the excess amount of oxygen vacancies which promote the surface oxygen chemisorptions. The doping of $Ce^{3+/4+}$, which has a similar radius as Mn^{2+} but different valence, can cause lattice defect, thus improve the O_2 storage capacity and increases the catalytic activity. In the initial conditions, a reduced Ce captures oxygen from gas-phase molecules and oxidizes by electron transfer from Ce^{3+} surface to adsorbed oxygen. Then, the oxygen of oxidized Ce was transferred into an active site on the catalyst surface therefore the Ce was get reduced. The addition of smaller amount of Ce into the CuMnOx catalyst increases their strength and interface between Ce species and Cu-Mn species, thus leading to increase of the binding energy.

The order of activity of different types of catalysts for CO oxidation was as follows: 2.5%CeCu Mn_8Ox_{FRC} > 3.0%$CeCuMn_8Ox_{FRC}$ > 2.0%$CeCuMn_8Ox_{FRC}$ > 1.5%$CeCuMn_8Ox_{FRC}$ > 1.0%$CeCuMn_8Ox_{FRC}$ > 0.5%$CeCuMn_8Ox_{FRC}$ > $CuMn_{8RC}$. After the activity test confirm that the 2.5%$CeCuMn_8Ox_{FRC}$ catalyst has higher catalytic activity for CO oxidation as compared to other catalysts. The products with different

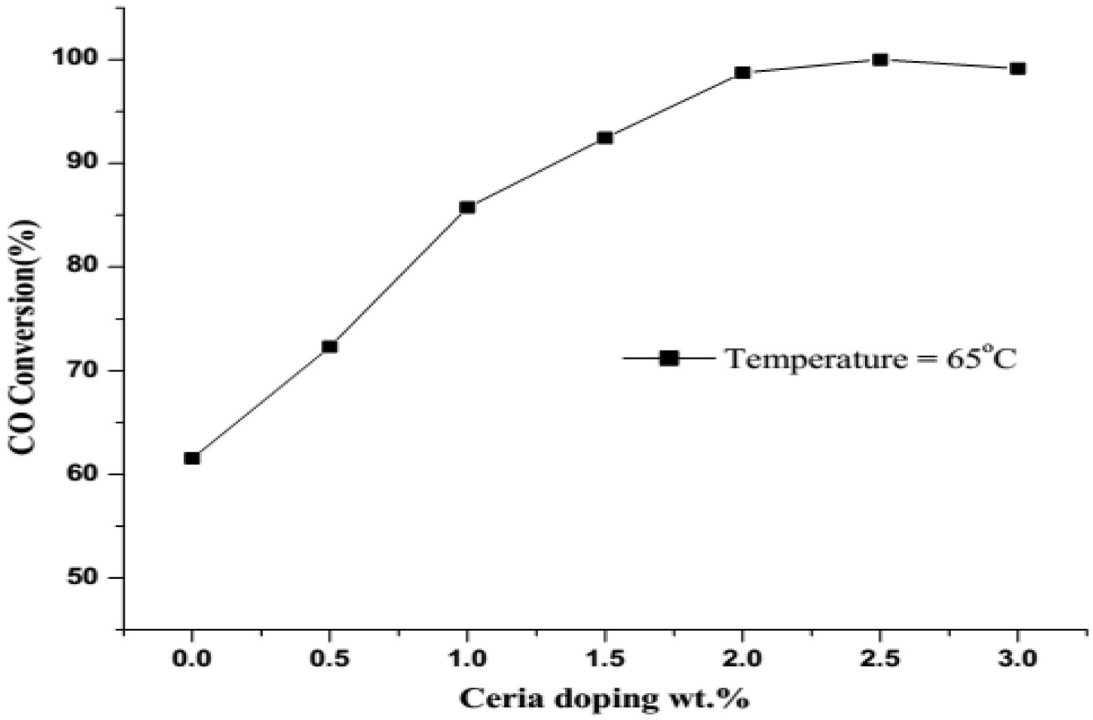

Fig. 14. Optimization wt.% Ce in $CuMn_{8RC}$ catalyst.

Table 10
Optimization of wt.% Ce in $CuMn_{8RC}$ catalyst.

Catalyst	CO Conversion (%)
$CuMn_{8RC}$	61.54%
$0.5\%CeCuMn_8Ox_{FRC}$	72.30%
$1.0\%CeCuMn_8Ox_{FRC}$	85.75%
$1.5\%CeCuMn_8Ox_{FRC}$	92.45%
$2.0\%CeCuMn_8Ox_{FRC}$	98.75%
$2.5\%CeCuMn_8Ox_{FRC}$	100%
$3.0\%CeCuMn_8Ox_{FRC}$	99.35%

ceria doping were evaluated for their catalytic activity towards CO oxidation reaction. Compared with traditional $CuMn_{8RC}$ catalyst, the Ce-doped $CuMn_8Ox_{RC}$ have better catalytic activity towards CO oxidation at a low temperature. This defective surface is supposed to provide enriched nucleation sites for the growth and improved dispersion of loaded metal. The morphology and structures of $CeCuMn_8Ox_{FRC}$ catalysts products change as the doping amount from 0.5 to 3 wt.% increases and so does the catalytic performance. The ceria was doped into the $CuMn_8Ox_F$ lattice successfully. The $2.5\%CeCuMn_8Ox_{FRC}$ catalyst has best catalytic performance among the series of products as most oxygen vacancies and large surface area. The role of different Ce species has also been studied, and Ce^{3+} as an active species was found to increase the catalytic activity at low temperatures. The addition of 2.5%Ce into the CuMnOx catalyst leads to an increase in the surface area and also increases the number of active sites present on the catalyst surface and further addition of ceria promoters in CuMnOx catalysts beyond 2.5 wt.% loading the activity of catalysts was made constant. These properties can be achieved by controlling the size, shape, particle size distribution, composition and electronic structure of surface, thermal and chemical stability of specific nanocomponents [76–78].

The CuMnOx catalyst has higher oxygen storage capacity, faster oxygen adsorption and oxide reduction rates than the present commercial ceria-stabilized alumina support. Based on the experimental result, it was found that the addition of ceria lowers the band gap of catalyst. In this case, the band gap was lowered and also excited electrons had potential high enough to oxidized CO [79,80]]. In the Ce doped CuMnOx catalyst presence of mixed oxides of Ce_2O_3 and CeO_2 are most enriched Ce^{3+} and Ce^{4+} has smallest size among all the cations present on surface [23–25,81]. The modification of ceria by doping in CuMnOx catalysts applied several benefits on the catalytic features of ceria such as improvement in the thermal stability, improved surface reducibility, high oxygen mobility, which contributes to the effective CO oxidation. The high lattice ion mobility and possibility of readily switching between Ce^{3+} and Ce^{4+}, together with the high oxidizing power of Ce^{4+} cation, ceria always represents special catalytic properties. The Ce^{3+} has a larger effective ionic radius than that of Ce^{4+}, thus the increase of Ce^{3+} would result in an expansion of CeO_2 lattice. In the initial conditions, a reduced Ce captures oxygen from the gas-phase molecules and oxidizes by electron transfer from the Ce^{3+} surface to the adsorbed oxygen in the ceria promoted CuMnOx catalysts. Then, the oxygen of oxidized Ce was transferred to an active site on the catalyst surface; therefore, the Ce was getting reduced. The structure and adsorption mechanisms of all sites on ceria promoted catalysts are active for CO chemisorptions [82–85]. Ceria particles preferentially expose stable (111) planes and reducing the particle size of ceria to nano-dimensions, contributions from the less stable (110) and (100) terminations. The CeO_2 (111) has an open structure with O in the top layer followed by present in Ce layer, whereas, on the (110) surface, both Ce and O atoms are in the top layer. The ceria promoted CuMnOx catalysts with low index surface planes and easy defect formation is desirable for catalytic applications. The surface defects such as a vacancy cluster, pits and high degree of surface roughness represent improved reactivity for CO oxidation [86–88]. The presence of bimodal particle size distribution, with smaller particles showing a lattice constant that is larger than bulk CeO_2. The lattice expansion can be caused by the presence of Ce^{3+} ions in this ionic lattice. The increased activity for CO oxidation could be attributed to the weakening of Ce-O bond and increased oxygen mobility. The ionic species in intimate contact with ceria lattice would act as a modifier of the ceria properties [89–91].

4.6. Stability test

The stability test of 2.5%CeCuMn$_8$Ox$_{FRC}$ catalyst was conducted at 65 °C for the oxidation of CO in a continuous running for 48 h under the earliest mentioned experimental conditions. The results represent that practically no deactivation of 2.5%CeCuMn$_8$Ox$_{FRC}$ catalyst has occurred in the experiments. The amazing performance of 2.5%CeCuMn$_8$Ox$_{FRC}$ catalyst produced by RC for CO oxidation was associated with the modification in intrinsic textural, morphological characteristics such as crystallite size, surface area and particle size of catalyst. The performance of this catalyst was judge by their activity, selectivity and stability. The catalytic behavior of Cu-Mn oxides catalysts that were suffering from a rapid deactivation by moisture in the oxidation of CO. The dynamics of catalyst surface during the reaction were essential to an understanding of the deactivation mechanism of Ce-based CuMn$_8$Ox$_F$ catalysts, as well as the role of Ce in stabilizing the 2.5%CeCuMn$_8$Ox$_{FRC}$ catalyst. The deactivation was formation of inactive oxidized surface Cu-Mn species under reaction conditions. The addition of smaller amount of Ce improves the stability of metallic Cu-Mn surface against oxidation, leading to significantly improved stability of 2.5%CeCuMn$_8$Ox$_{FRC}$ catalyst.

4.7. Mechanism of CO oxidation over ceria promoted CuMnOx catalyst

The efficiency of ceria promoted CuMnOx catalysts for reactions with stable CO molecules is strongly depending upon the chemisorptions process. The chemisorptions of reacting gases is an important step, which increases the concentration of reactant on the catalyst surfaces, it inducing the adsorbed CO molecules processing on high energy to get easy the chemical reactions. The reaction mechanism of CO oxidation over ceria promoted CuMnOx catalyst shows that the most accepted CO oxidation reaction on a catalyst surface that involves O_2 adsorption to form O_2* precursors, which split on a vicinal vacancy. The mechanism of reaction and rate expression much depends on the types of catalysts was used on their structure and surface properties [31–34]. The power-law and reaction rate law models frequently found to be sufficient enough for preface studies. The CO oxidation on the Cu-Mn-CeO_2 catalyst follows by a Mars-van Krevelen mechanism, in which the oxygen vacancies can be replenished by pretty active lattice oxygen. The successful collisions of CO molecules produce have enough energy and this energy also known as activation energy (Ea). The speed of CO molecules collision with the increasing of temperature produces more energy and this energy enough to reach the Ea, it causes increases in the overall reaction rate [35–38]. With the help of Arrhenius' equation, we have to calculate the minimum amount of activation energy (Ea) at an absolute temperature (T) required to complete oxidation of CO. The activation energy was obtained after kinetics study of 2.5%CeCuMn$_8$Ox$_{FRC}$ catalyst as a function of temperature 65 °C was 46KJ/g.mol, which was least as compared to the activation energy of CuMn$_8$Ox$_{RC}$ = 55 KJ/g.mol catalyst. The reaction order of all catalysts was found to be first order. The kinetics data were collected under condition of free heat and mass transfer limitations. In ceria promoted CuMnOx catalysts, the lattice oxygen in first few surface layers of ceria is transferred onto CO and gaseous O_2 fills up the vacancies created on oxide [40–42]. The oxygen exchange with lattice oxygen in CeO_2, then the high CO oxidation activity could be observed to the increased participation of lattice oxygen. The interface between Cu-Mn and ceria acts as an active oxygen to generate active oxygen species, which may further react with CO and thus catalyze the reaction. The crystal size of CeO_2 grows rapidly at the higher temperatures, while the size of doped ceria grows much milder in constant at wide range temperatures. The molecular oxygen adsorbs at these vacancies and forms O species then catalyze the oxidation of CO closing the catalytic cycle and recovering the stoichiometric $M_xCe_{1-x}O_2$ system [43–45].

5. Conclusion

The structure and catalytic properties of Ce-doped CuMn$_8$Ox catalysts were closely related to the Ce content. Doping with 2.5% (molar percentage) Ce significantly improved the catalytic property, and made Cu and Mn components uniformly distribute in the catalyst. The catalyst exhibited a synergistic effect in increasing the surface of Cu-Mn dispersion, consequently, it showed higher catalytic activity in lower temperatures. Physical characterizations of catalysts represents that the beneficial effect of Ce dopant on CuMn$_8$Ox$_F$ can be linked to the good intimate contact of dopants with the catalyst have a high surface area and small particle size. The activity order of catalysts for CO oxidation was as follows: 2.5%CeCuMn$_8$Ox$_F$ > CuMn$_8$Ox$_F$. The calcinations order with respect to the performance of catalysts for CO oxidation was as follows: reactive calcination > flowing air > stagnant air. The performance of catalysts was in accordance with their characterization. As a catalyst with lower cost and better catalytic efficiency, the ceria doped CuMn$_8$Ox has potential applications for CO oxidation. Spent 2.5%CeCuMn$_8$Ox catalyst was a very important secondary resource for metal recovery and low-temperature CO oxidation. This paper study of Spent 2.5%CeCuMn$_8$Ox catalyst by their characterization value and compared with fresh catalyst characterization. If the spent 2.5%CeCuMn$_8$Ox catalysts can be regenerated and activated effectively, they can be reused with higher values and economic efficiency.

References

[1] B.F.F. Benjamin, P. Alphonse, Co-Mn-oxide spinel catalysts for CO and propane oxidation at mild temperature, Appl. Catal. B Environ. 180 (2016) 715–724.
[2] L. Cai, Y. Guo, A. Lu, P. Branton, W. Li, The choice of precipitant and precursor in the co-precipitation synthesis of copper manganese oxide for maximizing carbon monoxide oxidation, J. Mol. Catal. A Chem. 360 (2012) 35–41.
[3] V.D.B.C. Dasireddy, J. Valand, B. Likozar, PROX reaction of CO in $H_2/H_2O/CO_2$ water gas shift (WGS) feed stocks over CueMn/Al2O3 and CueNi/Al2O3 catalysts for fuel cell applications, Renew. Energy 116 (2018) 75–87.
[4] S. Dey, G.C. Dhal, D. Mohan, R. Prasad, Characterization and activity of CuMnOx/γ-Al_2O3 catalyst for oxidation of carbon monoxide, Mater. Discov. 8 (2017) 26–34.
[5] S. Dey, G.C. Dhal, D. Mohan, R. Prasad, Copper based mixed oxide catalysts (CuMnCe, CuMnCo and CuCeZr) for the oxidation of CO at low temperature, Mater. Discov. 10 (2017) 1–14.
[6] S. Dey, G.C. Dhal, D. Mohan, R. Prasad, Effect of preparation conditions on the catalytic activity of CuMnOx catalysts for CO oxidation, Bull. Chem. React. Eng. Catal. 12 (3) (2017) 1–15.
[7] S. Dey, G.C. Dhal, D. Mohan, R. Prasad, Kinetics of catalytic oxidation of carbon monoxide over CuMnAgOx catalyst, Mater. Discov. 8 (2017) 18–25.
[8] S. Dey, G.C. Dhal, D. Mohan, R. Prasad, Low-temperature complete oxidation of CO over various manganese oxide catalysts, Atmos. Pollut. Res. 9 (2018) 755–763.
[9] R.T. Dong, H.L. Wang, Q. Zhang, X.T. Xu, F. Wang, B. Li, Shape-controlled synthesis of Mn_2O3 hollow structures and their catalytic properties, CrystEngComm 17 (2015) 7406–7413.
[10] S. Dey, G.C. Dhal, D. Mohan, R. Prasad, Study of Hopcalite (CuMnOx) catalysts prepared through a novel route for the oxidation of carbon monoxide at low temperature, Bull. Chem. React. Eng. Catal. 12 (3) (2017) 393–407.
[11] S. Dey, G.C. Dhal, D. Mohan, R. Prasad, Synthesis and characterization of $AgCoO_2$ catalyst for oxidation of CO at a low temperature, Polyhedron 155 (2018) 102–113.
[12] S. Dey, G.C. Dhal, D. Mohan, R. Prasad, The choice of precursors in the synthesizing of CuMnOx catalysts for maximizing CO oxidation, Int. J. Ind. Chem. 9 (2018) 199–214.
[13] S. Dey, G.C. Dhal, D. Mohan, R. Prasad, R.N. Gupta, Cobalt doped CuMnOx catalysts for the preferential oxidation of carbon monoxide, Appl. Surf. Sci. 441 (2018) 303–316.
[14] S. Dey, G.C. Dhal, R. Prasad, D. Mohan, Effect of nitrate metal (Ce, Cu, Mn and Co) precursors for the total oxidation of carbon monoxide, Resour. Effic. Technol. 3 (2016) 293–302.
[15] S. Dey, G.C. Dhal, R. Prasad, D. Mohan, Effects of doping on the performance of CuMnOx catalyst for CO oxidation, Bull. Chem. React. Eng. Catal. 12 (3) (2017) 1–14.
[16] Z.H. Dong, X.Y. Lai, J.E. Halpert, N.L. Yang, L.X. Yi, J. Zhai, D. Wang, Z.Y. Tang, L. Jiang, Accurate control of multishelled ZnO hollow microspheres for dye-sensitized solar cells with high efficiency, Adv. Mater. 24 (2012) 1046–1049.
[17] A. Elmhamdi, L. Pascual, K. Nahdi, A. Martínez-Arias, Structure/redox/activity relationships in $CeO_2/CuMn_2O4$ CO-PROX catalysts, Appl. Catal. B Environ. 217 (2017) 1–11.
[18] A. Faiz, C.S. Weaver, M.P. Walsh, Air Pollution from Motor Vehicles, Standards and Technologies for Controlling Emissions, The World Bank Reconstruction and Development, Washington DC, 1996.
[19] J. Gao, C. Jia, L. Zhang, H. Wang, Y. Yang, S. Hung, Y. Hsu, B. Liu, Tuning chemical

bonding of MnO_2 through transition-metal doping for enhanced CO oxidation, J. Catal. 341 (2016) 82–90 2016.
[20] Gao, Y., Wu, X., Liu, S., Weng, D. and Ran, R.2018. MnOx–CeO2 Mixed Oxides for Diesel Soot Oxidation: A Review. Catalysis Surveys from Asia10.1007/s10563-018-9255-4.
[21] X. Guo, J. Li, R. Zhou, Catalytic performance of manganese doped CuO-CeO_2 catalysts for selective oxidation of CO in hydrogen-rich gas, J. Fuel 20 (2016) 56–64.
[22] Y. Guo, C. Li, S. Lu, C. Zhao, Low temperature CO catalytic oxidation and kinetic performances of KOH–Hopcalite in the presence of CO_2, RSC Adv. 6 (2016) 7181–7188.
[23] Y. Hasegawa, R. Maki, M. Sano, T. Miyake, Preferential oxidation of CO on copper-containing manganese oxides, Appl. Catal. A Gen. 371 (2009) 67–72.
[24] Y. Hong, S. Zhang, F.T. Tao, Y. Wang, Stabilization of iron-based catalysts against oxidation: an in situ ambient-pressure X-ray photoelectron spectroscopy (AP-XPS) study, Am. Chem. Soc. Catal. 7 (2017) 3639–3643.
[25] J.A. Hoskins, Carbon monoxide: the unnoticed poison of the 21 st century, Indoor Built Environ. 8 (1999) 154–155.
[26] W.M. Hoskins, W.C. Bray, The catalytic oxidation of carbon monoxide. II. The adsorption of carbon dioxide, carbon monoxide and oxygen by the catalysts, manganese dioxide, cupric oxide and mixtures of these oxides, J. Am. Chem. Soc. 48 (6) (1926) 1454–1474.
[27] C. Jones, K.J. Cole, S.H. Taylor, M.J. Crudace, G.J. Hutchings, Copper manganese oxide catalysts for ambient temperature carbon monoxide oxidation: effect of calcination on activity, J. Mol. Catal. A Chem. 305 (2009) 121–124.
[28] Jones, C.D.2006. The Ambient Temperature Oxidation of Carbon Monoxide by Copper-Manganese Oxide Based Catalysts. Ph.D. Thesis, Cardiff Catalysis Institute, Cardiff University, UK.
[29] M. Katz, The heterogeneous oxidation of carbon monoxide, Adv. Catal. 5 (1953) 177–216.
[30] V.T. Kumar, D.N. Durgasri, S. Maloth, B.M. Reddy, Tuning the structural and catalytic properties of ceria by doping with Zr^{4+}, La^{3+} and Eu^{3+} cations, J. Chem. Soc. 127 (7) (2015) 1145–1153.
[31] J. Lee, H. Kim, H. Lee, S. Jang, J.H. Chang, Highly efficient elimination of carbon monoxide with binary copper-manganese oxide contained ordered nanoporous silicas, Nanoscale Res. Lett. 11 (2016) 2–6.
[32] Z. Li, H. Wang, X. Wu, Q. Ye, X. Xu, B. Li, F. Wang, Novel synthesis and shape-dependent catalytic performance of Cu–Mn oxides for CO oxidation, Appl. Surf. Sci. 403 (2017) 335–341.
[33] S. Liu, X. Wu, W. Liu, D. Weng, Soot oxidation over CeO_2 and Ag/CeO_2: factors determining the catalyst activity and stability during reaction, J. Catal. 337 (2016) 188–198.
[34] T. Montini, M. Melchionna, M. Monai, P. Fornasiero, Fundamentals and catalytic applications of CeO_2-based materials, Chem. Rev. 116 (10) (2016) 5987–6041.
[35] E.C. Njagi, C. Chen, H. Genuino, H. Galindo, H. Huang, S.L. Suib, Total oxidation of CO at ambient temperature using copper manganese oxide catalysts prepared by a redox method, Appl. Catal. A Gen. 99 (2010) 103–110.
[36] V.M. Orera, R.I. Merino, F. Pena, $Ce^{3+} \leftrightarrow Ce^{4+}$ conversion in ceria-doped zirconia single crystals induced by oxidoreduction treatments, Solid State Ionics 72 (2) (1994) 224–231.
[37] C.T. Peng, H.K. Lia, B.J. Liaw, Y.Z. Chen, Removal of CO in excess hydrogen over CuO/Ce_{1-x} MnXo2 catalysts, Chem. Eng. J. 172 (2011) 452–458.
[38] U.R. Pillai, S. Deevi, Room temperature oxidation of carbon monoxide over copper oxide catalyst, Appl. Catal. B Environ. 64 (1–2) (2006) 146–151.
[39] R. Prasad, P. Singh, A novel route of single step reactive calcination of copper salts far below their decomposition temperatures for synthesis of highly active catalysts, Catal. Sci. Technol. 3 (2013) 3326–3334.
[40] K. Qian, Z. Qian, Q. Hua, Z. Jiang, W. Huang, Structure activity relationship of CuO/MnO_2 catalysts in CO oxidation, Appl. Surf. Sci. 273 (2013) 357–363.
[41] M. Reli, N. Ambrozová, M. Sihor, L. Matejová, L. Capek, L. Obalová, Z. Matej, A. Kotarba, K. Kocí, Novel cerium doped titania catalysts for photocatalytic decomposition of ammonia, Appl. Catal. B Environ. 178 (2015) 108–116.
[42] J.A. Rodriguez, D.C. Grinter, Z. Liu, R.M. Palomino, S.D. Senanayake, Ceria-based model catalysts: fundamental studies on the importance of the metal–ceria interface in CO oxidation, the water–gas shift, CO_2 hydrogenation and methane and alcohol reforming, Chem. Soc. Rev. 46 (7) (2017) 1824–1841.
[43] M. Roy, S. Basak, M.K. Naskar, Bi-template assisted synthesis of mesoporous manganese oxide nanostructures: tuning properties for efficient CO oxidation, Phys. Chem. Chem. Phys. 18 (2016) 5253–5263.
[44] L. Shi, Z. Hu, G. Deng, W. Li, Carbon monoxide oxidation on copper manganese oxides prepared by selective etching with ammonia, Chin. J. Catal. 36 (2015) 1920–1927.
[45] P. Singh, R. Prasad, Catalytic abatement of cold start vehicular CO emissions, Catal. Ind. 6 (2) (2014) 122–127.
[46] B. Solsona, G.J. Hutchings, T. Garcia, S.H. Taylor, Improvement of the catalytic performance of CuMnOx catalysts for CO oxidation by the addition of Au, N. J. Chem. 28 (2004) 708–711.
[47] S.S.P. Sultana, D.H.V. Kishore, M. Kuniyil, M. Khan, A. Alwarthan, K.R.S. Prasad, J.P. Labis, S.F. Adi, Ceria doped mixed metal oxide nanoparticles as oxidation catalysts: synthesis and their characterization, Arab. J. Chem. 8 (6) (2015) 766–770.
[48] W.X. Tang, X.F. Wu, S.D. Li, X. Shan, G. Liu, Y.F. Chen, Co-nanocasting synthesis of mesoporous Cu–Mn composite oxides and their promoted catalytic activities for gaseous benzene removal, Appl. Catal. B 162 (2015) 110–121.
[49] S.H. Taylor, G.J. Hutchings, A.A. Mirzaei, Copper zinc oxide catalysts for ambient temperature carbon monoxide oxidation, Chem. Commun. 1 (1999) 1373–1374.
[50] S. Trivedi, R. Prasad, Choice of precipitant and calcination temperature of precursor for synthesis of $NiCo_2O4$ for control of CO–CH_4 emissions from CNG vehicles, J. Environ. Sci. 65 (2017) 1–10.
[51] C.C. Yec, H.C. Zeng, Synthesis of complex nanomaterials via Ostwald ripening, J. Mater. Chem. A 2 (2014) 4843–4851.
[52] X. Zhang, K. Ma, L. Zhang, G. Yong, Y. Dai, S. Liu, Effect of precipitation method and Ce doping on the catalytic activity of copper manganese oxide catalysts for CO oxidation, Chin. J. Chem. Phys. 24 (2010) 97–102.
[53] J. Bub, D. Solenov, Microscopic origin of interaction between oxygen and fluorine adsorbates covalently bound to graphene, Surf. Interfaces 17 (2019) 100354.
[54] M.A.M. Ibrahim, Bakdash, Copper-rich Cu–Zn alloy coatings prepared by electro deposition fromglutamate complex electrolyte: morphology, structure, micro hardness and electrochemical studies, Surf. Interfaces 18 (2020) 100404.
[55] K. Furukawa, K. Wagatsuma, Formation of an oxide layer on a biomaterial Co-Cr-Mo alloy by using a hollow-cathode glow discharge plasma with argon-oxygen and neon-oxygen mixed gases, Surf. Interfaces 18 (2020) 100402.
[56] P. Arunarajeswari, T. Mathavan, A. Divya, A.M.F. Benial, Synthetic approach of organic acid assisted δ-Al_2O3 nanorods toward engineering surface chemistry, Surf. Interfaces 18 (2020) 100421.
[57] K. Ravichandran, A.J. Santhosam, M. Sridharan, Effect of tungsten doping on the ammonia vapour sensing ability of ZnO thin films prepared by a cost effective simplified spray technique, Surf. Interfaces 18 (2020) 100412.
[58] F.Z. Akika, M. Benamira, H. Lahmar, M. Trari, I. Avramova, S. Suzer, Structural and optical properties of Cu-doped $ZnAl_2O4$ and its application as photocatalyst for Cr (VI) reduction under sunlight, Surf. Interfaces 18 (2020) 100406.
[59] X. Zhang, Q. Huang, M. Liu, J. Tian, G. Zeng, Z. Li, K. Wang, Q. Zhang, Q. Wan, F. Deng, Y. Wei, Preparation of amine functionalized carbon nanotubes via a bio inspired strategy and their application in Cu^{2+} removal, Appl. Surf. Sci. 343 (2015) 19–27.
[60] Q. Huang, M. Liu, J. Chen, Q. Wan, J. Tian, L. Huang, R. Jiang, Y. Wen, X. Zhang, Y. Wei, Facile preparation of MoS_2 based polymer composites via mussel inspired chemistry and their high efficiency for removal of organic dyes, Appl. Surf. Sci. 419 (2017) 35–44.
[61] Q. Huang, M. Liu, J. Zhao, J. Chen, G. Zeng, H. Huang, J. Tian, Y. Wen, X. Zhang, X. Wei, Facile preparation of polyethylenimine-tannins coated SiO_2 hybrid materials for Cu^{2+} removal, Appl. Surf. Sci. 427 (2018) 535–544.
[62] Q. Huang, M. Liu, L. Mao, D. Xu, G. Zeng, H. Huang, R. Jiang, F. Deng, X. Zhang, Y. Wei, Surface functionalized SiO_2 nanoparticles with cationic polymers via the combination of mussel inspired chemistry and surface initiated atom transfer radical polymerization: characterization and enhanced removal of organic dye, J. Colloid Interface Sci. 499 (2017) 170–179.
[63] X. Zhang, Q. Huang, F. Deng, H. Huang, Q. Wan, M. Liu, Y. Wei, Mussel-inspired fabrication of functional materials and their environmental applications: progress and prospects, Appl. Mater. Today 7 (2017) 222–238.
[64] Q. Huang, J. Zhao, M. Liu, Y. Li, J. Ruan, Q. Li, J. Tian, X. Zhu, X. Zhang, Y. Wei, Synthesis of polyacrylamide immobilized molybdenum disulfide (MoS_2@PDA @ PAM) composites via mussel-inspired chemistry and surface-initiated atom transfer radical polymerization for removal of copper(II) ions, J. Taiwan Inst. Chem. Eng. 86 (2018) 174–184.
[65] Q. Huang, J. Zhao, M. Liu, J. Chen, X. Zhu, T. Wu, J. Tian, Y. Wen, X. Zhang, Y. Wei, Preparation of polyethylene polyamine@ tannic aciden capsulated MgAl-layered double hydroxide for the efficient removal of copper(II)ions from aqueous solution, J. Taiwan Inst. Chem. Eng. 82 (2018) 92–101.
[66] G. Zeng, T. Chen, L. Huang, M. Liu, R. Jiang, Q. Wan, Y. Dai, Y. Wen, X. Zhang, Y. Wei, Surface modification and drug delivery applications of MoS_2 nanosheets with polymers through the combination of mussel inspired chemistry and SET-LRP, J. Taiwan Inst. Chem. Eng. 82 (2018) 205–213.
[67] G. Zeng, X. Liu, M. Liu, Q. Huang, D. Xu, Q. Wan, H. Huang, F. Deng, X. Zhang, Y. Wei, Facile preparation of carbon nanotubes based carboxymethyl chitosa nnano composites through combination of mussel inspired chemistry and Michael addition reaction: characterization and improved Cu^{2+} removal capability, J. Taiwan Inst. Chem. Eng. 68 (2016) 446–454.
[68] S. Dey, G.C. Dhal, Cerium catalysts applications in carbon monoxide oxidations, Mater. Sci. Energy Technol. 3 (2020) 6–24.
[69] S. Dey, G.C. Dhal, D. Mohan, R. Prasad, Application of hopcalite catalyst for controlling carbon monoxide emission at cold-start emission conditions, J. Traffic Transp. Eng. Engl. Ed. 6 (5) (2019) 419–440.
[70] Y. Liu, H. Huang, D. Gan, L. Guo, M. Liu, J. Chen, F. Deng, N. Zhou, X. Zhang, Y. Wei, A facile strategy for preparation of magnetic graphene oxide composites and their potential for environmental adsorption, Ceram. Int. 44 (15) (2018) 18571–18577.
[71] J. Dou, D. Gan, Q. Huang, M. Liu, J. Chen, F. Deng, X. Zhu, Y. Wen, X. Zhang, Y. Wei, Fictionalization of carbon nanotubes with chitosan based on MALI multi component reaction for Cu^{2+} removal, Int. J. Biol. Macromol. 136 (2019) 476–485.
[72] S. Dey, G.C. Dhal, Materials progress in the control of CO and CO_2 emission at ambient conditions: an overview, Mater. Sci. Energy Technol. 2 (2019) 607–623.
[73] S. Dey, G.C. Dhal, Applications of silver nanocatalysts for low-temperature oxidation of carbon monoxide, Inorg. Chem. Commun. 110 (2019) 107614.
[74] D. Gan, M. Liu, H. Huang, J. Chen, J. Dou, Y. Wen, Q. Huang, Z. Yang, X. Zhang, Y. Wei, Facile preparation of functionalized carbon nanotubes with tannins through mussel-inspired chemistry and their application in removal of methylene blue, J. Mol. Liq. 271 (2018) 246–253.
[75] S. Dey, G.C. Dhal, D. Mohan, R. Prasad, Synthesis of silver promoted CuMnOx catalyst for ambient temperature oxidation of carbon monoxide, J. Sci. Adv. Mater. Dev. 4 (2019) 47–56.
[76] Y. Lei, Y. Cui, Q. Huang, J. Dou, D. Gan, F. Deng, M. Liu, X. Li, X. Zhang, Y. Wei, Facile preparation of sulfonic groups functionalized MXenes for efficient removal of

methylene blue, Ceram. Int. 45 (14) (2019) 17653–17661 2019.
[77] S. Dey, G.C. Dhal, A review of synthesis, structure and applications in hopcalite catalysts for carbon monoxide oxidation, Aerosol Sci. Eng. (2019), https://doi.org/10.1007/s41810-019-00046-1.
[78] S. Dey, G.C. Dhal, Deactivation and regeneration of hopcalite catalyst for carbon monoxide oxidation: a review, Mater. Today Chem. 14 (2019) 100180.
[79] Y. Liu, K. Ai, L. Lu, Polydopamine and its derivative materials: synthesis and promising applications in energy, environmental and biomedical fields, Chem. Rev. 114 (9) (2014) 5057–5115.
[80] S. Dey, G.C. Dhal, The catalytic activity of cobalt nanoparticles for low-temperature oxidation of carbon monoxide, Mater. Today Chem. 14 (2019) 100198.
[81] X. Zhang, Q. Huang, F. Deng, H. Huang, Q. Wan, M. Liu, Y. Wei, Mussel-inspired fabrication of functional materials and their environmental applications: progress and prospects, Appl. Mater. Today 7 (2017) 222–238.
[82] S. Dey, G.C. Dhal, D. Mohan, R. Prasad, Effect of various metal oxides phases present in CuMnOx catalyst for selective CO oxidation, Mater. Discov. 12 (2018) 63–71.
[83] M. Liu, G. Zeng, K. Wang, Q. Wan, L. Tao, X. Zhang, Y. Wei, Recent developments in polydopamine: an emerging soft matter for surface modification and biomedical applications, Nanoscale 8 (38) (2016) 16819–16840.
[84] Dey, S., Dhal, G.C., Mohan, D. and Prasad, R.2019. Advances in Transition Metal Oxide Catalysts for Carbon Monoxide Oxidation: A Review Advanced Composites and Hybrid Materials2(4), 626–656.
[85] S. Dey, G.C. Dhal, D. Mohan, R. Prasad, Synthesis of highly active cobalt catalysts for low temperature CO oxidation, Chem. Data Collect. 24 (2019) 100283.
[86] S. Dey, G.C. Dhal, D. Mohan, R. Prasad, Ambient temperature complete oxidation of carbon monoxide using hopcalite catalysts for fire escape masks applications, Adv. Compos. Hybrid Mater. 2 (3) (2019) 501–519.
[87] S. Dey, G.C. Dhal, Highly active palladium nanocatalysts for low-temperature carbon monoxide oxidation, Polytechnica (2019), https://doi.org/10.1007/s41050-019-00018-x.
[88] M. Liu, J. Ji, X. Zhang, X. Zhang, B. Yang, F. Deng, Z. Li, K. Wang, Y. Yang, Y. Wei, Self-polymerization of dopamine and polyethyleneimine: novel fluorescent organic nanoprobes for biological imaging applications, J. Mater. Chem. B 3 (17) (2015) 3476–3482.
[89] Y. Shi, M. Liu, F. Deng, G. Zeng, Q. Wan, X. Zhang, Y. Wei, Recent progress and development on polymeric nanomaterials for photothermal therapy: a brief overview, J. Mater. Chem. B 5 (2) (2017) 194–206.
[90] Y. Shi, R. Jiang, M. Liu, L. Fu, G. Zeng, Q. Wan, L. Mao, F. Deng, X. Zhang, Y. Wei, Facile synthesis of polymeric fluorescent organic nanoparticles based on the self-polymerization of dopamine for biological imaging, Mater. Sci. Eng. C 77 (2017) 972–977.
[91] L. Huang, M. Liu, H. Huang, Y. Wen, X. Zhang, Y. Wei, Recent advances and progress on melanin-like materials and their biomedical applications, Biomacromolecules 19 (6) (2018) 1858–1868.